MICRO-MINIATURE ROLL RATE SENSOR

Jonathan Grant
Bruce Nelson
George Garnes
GEO-CENTERS, INC.
7 Wells Avenue
Newton Centre, MA 02159
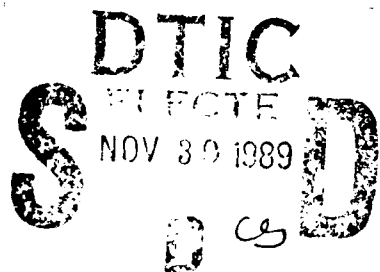
Phillip E. Houser
Project Engineer
ARDEC

November 17, 1989

U.S. ARMY ARMAMENT RESEARCH, DEVELOPMENT AND ENGINEERING CENTER

Fire Support Armaments Center

Picatinny Arsenal, New Jersey

US ARMY
ARMAMENT MUNITIONS
& CHEMICAL COMMAND
ARMAMENT RDE CENTER

REPORT DOCUMENTATION PAGE

1a REPORT SECURITY CLASSIFICATION	1b RESTRICTIVE MARKINGS
UNCLASSIFIED	

2a SECURITY CLASSIFICATION AUTHORITY	3 DISTRIBUTION / AVAILABILITY OF REPORT
2b DECLASSIFICATION / DOWNGRADING SCHEDULE	Approved for public release; distribution is unlimited.

4 PERFORMING ORGANIZATION REPORT NUMBER(S)	5. MONITORING ORGANIZATION REPORT NUMBER(S)
GC-89-FR-1702-002	Contractor Report ARFSD-CR-89018

6a NAME OF PERFORMING ORGANIZATION	6b. OFFICE SYMBOL (If applicable)	7a. NAME OF MONITORING ORGANIZATION
GEO-CENTERS, INC.		ARDEC, FSAC

6c ADDRESS (City, State, and ZIP Code)	7b. ADDRESS (City, State, and ZIP Code)
7 Wells Avenue Newton Centre, MA 02159	Precision Munitions Division (SMCAR-FSP-A) Picatinny Arsenal, NJ 07806-5000

8a. NAME OF FUNDING / SPONSORING ORGANIZATION ARDEC, IMB STINFO Br	8b OFFICE SYMBOL (If applicable) SMCAR-IMI-I	9 PROCUREMENT INSTRUMENT IDENTIFICATION NUMBER DAAA21-87-C-0066

8c ADDRESS (City, State, and ZIP Code)	10 SOURCE OF FUNDING NUMBERS			
Picatinny Arsenal, NJ 07806-5000	PROGRAM ELEMENT NO	PROJECT NO	TASK NO	WORK UNIT ACCESSION NO

11 TITLE (Include Security Classification)

MICRO-MINIATURE ROLL RATE SENSOR

12 PERSONAL AUTHOR(S) J.F. Grant, B.N. Nelson, G.W. Garnes, GEO-CENTERS, INC. and Phillip E. Houser, Project Engineer, ARDEC

13a TYPE OF REPORT	13b TIME COVERED	14. DATE OF REPORT (Year, Month, Day)	15. PAGE COUNT
Final	FROM 3/87 TO 8/89	89 November 17	74

16 SUPPLEMENTARY NOTATION

17	COSATI CODES		18 SUBJECT TERMS (Continue on reverse if necessary and identify by block number)
FIELD	GROUP	SUB-GROUP	Rate sensing, Rotation sensing, Optical sensors, Accelerometers

19 ABSTRACT (Continue on reverse if necessary and identify by block number)

The Phase II "Micro-Miniature Roll Rate Sensor Program" developed an optical centripetal accelerometer that can be tailored to work over a wide range of accelerations. A rate sensing device was developed by measuring centripetal acceleration due to rotation with a proof mass loading a photoelastic sensing element. The acceleration is proportional to the amount of birefringence induced by the load. Development of this technology resulted in construction of a prototype rate sensor targeted for use with the Copperhead munition. The sensors developed in this program can be adjusted for the desired range of operation through changes in width of a photoelastic (plastic) sensing element and/or changes in the amount of proof mass used to load the sensing element. Radial location of the sensor can also be used to control the range.

20. DISTRIBUTION / AVAILABILITY OF ABSTRACT	21. ABSTRACT SECURITY CLASSIFICATION
☐ UNCLASSIFIED/UNLIMITED ☒ SAME AS RPT ☐ DTIC USERS	UNCLASSIFIED

22a. NAME OF RESPONSIBLE INDIVIDUAL	22b. TELEPHONE (Include Area Code)	22c. OFFICE SYMBOL
I. Haznedari	(201) 724-3316	SMCAR-IMI-I

CONTENTS

TABLES

A-1

ii

FIGURES

iii

FIGURES (Continued)

FIGURES (Contined)

INTRODUCTION

This report documents a 24-month Phase II SBIR program by GEO-CENTERS, INC. to develop a Micro-miniature Roll Rate Sensor (MRRS) based on the photoelastic effect. The sensor detects changes in the polarization of light propagating through a photoelastic sensing element due to forces caused by centripetal acceleration associated with rotation. This work was sponsored by the U.S. Army Armament Research and Development Engineering Center to develop an alternate rate sensor for the Copperhead munition. The goal of this program was to develop alternate, cost effective methods to determine the rate of spin of projectiles.

BACKGROUND AND TASK OBJECTIVES

A roll rate sensor is a critical component in the design of smart, cannon launched munitions. Existing roll rate sensor designs are expensive, displace relatively large volumes, and require significant power for reliable operation. Such rate sensors depend heavily on precise alignment to the roll axis and special consideration must be paid to the mounting design to insure survival under severe launch conditions. Thus, the need exists to develop a lightweight, compact, rugged, low-power roll rate sensor whose performance is equivalent or superior to those currently in use.

The state-of-the-art in computer technology and fiber optic data communications imply that fiber optic rate sensors will be ultimately used in inertial guidance systems. Traditional mechanical strapdown sensors are too large, are unreliable and lack the required dynamic range and precision. For complete compatibility

1

with fiber optic data communications to the onboard computer, the output of a rate sensor should ideally be optical to preclude redundant analog to digital to optical conversions. Traditional sensor designs lack this significant trait which is inherent to fiber optic-based sensor designs.

The fundamental objective of the Phase II effort is to further develop the unique advantages and capabilities of extrinsic, photoelastic fiber optic rate sensors which were demonstrated during the Phase I contract. The photoelastic fiber optic sensor, which is an alternative approach to intrinsic fiber optic sensors, can be effectively used to measure a stress in a sensing element resulting from angular rotation. The proof-of-principle experiments completed during the Phase I effort demonstrated the viability of the based approach. Efforts through the first 12 months of the contract expanded on the Phase I research through evaluation of a matrix of materials and mechanical parameters. This evaluation has been performed with a roll rate sensor test bed to demonstrate the performance of final prototype designs. During the second 12 months of the program prototype MRRS were designed, built, and tested. The design of the prototype MRRS was based on the experimental data obtained during the first twelve months of the program, along with the requirements imposed by the Copperhead guided munition.

Sensor Performance Criteria

The roll rate sensor demonstrated during the Phase II program can be tailored for a range of performance capabilities through selection of the appropriate sensing element geometry, material and proof mass. Roll rate sensors are a critical component of the

2

Copperhead guided munition, and the specifications for rate sensing in the Copperhead were used as performance criteria for development of the MRRS. These criteria dictate that the sensor provide a roll rate output for a minimum range of 0-2000 deg/sec. The specifications used for the development of the prototype MRRS are given in the Configuration Item Development Specification, included as Appendix A.

TECHNICAL APPROACH

The MRRS is basically an optical accelerometer configured to measure radial acceleration. This is accomplished by loading an optical stress sensor with a proof mass having a freedom of movement only in the radial direction. The stress sensor is a birefringent sensing element that is probed with polarized light. Changes in polarization can be directly correlated to the centripetal acceleration of the proof mass due to angular rotation. From this, the angular velocity (rate) is easily determined. This technique uses one moving part (the proof mass) and inexpensive optical components. Due to the miniature size of the components, multiple sensors with averaged outputs can be utilized to ensure only radial (and not lateral) acceleration affects the calculated angular velocity. The theoretical operation of the sensor is discussed in detail in the following sections.

Photoelastic Effort Theory

The photoelastic effect can be utilized in a fiber optic sensor to detect stress. Figure 1 shows a schematic layout of the components and their orientation for a fiber optic stress sensor. When the photoelastic material is stressed in the x direction, the

3

index of refraction increases along that direction, while the index of refraction along the y direction remains constant. A beam of light polarized along the x direction propagates at a slower speed than a beam of light polarized along the y direction. Consequently, the x axis is known as the slow axis and the y axis is known as the fast axis. If light is initially polarized at $\pi/4$ with respect to these axes, then a phase shift will occur between the components of light that lie along each of these axes. This phase shift is proportional to the magnitude of the applied stress and the material thickness, and is referred to as stress induced birefringence.

With the sensor configuration shown in Figure 1, a change in the applied stress results in a change in optical transmission, which results in changed light intensities incident on the optical detectors. For this configuration, the output intensity for the $\pi/4$ and the $-\pi/4$ orientations is given by:

$$I_{\pi/4} = I_0 \sin^2 (\Gamma(S)/2 - \pi/4) \qquad (1)$$
$$I_{-\pi/4} = I_0 \sin^2 (\Gamma(S)/2 + \pi/4) \qquad (2)$$

where:

I_0 = input optical intensity

$\Gamma(S)$ = stress induced birefringence

The induced birefringence in an isotropic photoelastic material as a function of the applied stress is given by:

$$\Gamma(S) = (2\pi t/f) S \qquad (3)$$

4

where:

        t = the optical thickness of the photoelastic material (in)

        f = a material constant (psi/fringe/in)

        S = the applied stress (psi)

Equation (3) shows that the stress induced birefringence, and therefore, the sensor sensing range and sensitivity are dependent on the material geometry.

Equations (1) and (2) can be re-expressed in the following form:

$$I_{\pi/4} = I_0/2 - I_0 \sin \Gamma(S)/2 \cos \Gamma(S)/2 \tag{4}$$

$$I_{-\pi/4} = I_0/2 + I_0 \sin \Gamma(S)/2 \cos \Gamma(S)/2 \tag{5}$$

This allows the sum and difference of these two equations to be written as follows:

$$I_{sum} = I_{\pi/4} + I_{-\pi/4} = I_0 \tag{6}$$

$$I_{diff} = I_{-\pi/4} - I_{\pi/4} = 2I_0 \sin \Gamma(S)/2 \cos \Gamma(S)/2 \tag{7}$$

The sum-difference sensor output becomes:

$$\text{sum-difference} = \frac{I_{diff}}{I_{sum}} = 2 \sin \Gamma(S)/2 \cos \Gamma(S)/2$$

$$= \sin \Gamma(S) \tag{8}$$

Equation (8) shows that the sum-difference sensor output is intensity invariant, making this the preferred output detection

scheme for operating a fiber optic pressure sensor in environments where light intensity variations or radiation darkening of the fiber might occur.

Application of the Photoelastic Effect to Rotation Sensing

The photoelastic effect can also be used to sense centripetal acceleration. Figure 2 shows a schematic of the optical components for a rotation rate sensor. In this configuration, a proof mass is used to load a photoelastic material as it experiences centripetal acceleration. Equation (3) for this configuration reduces to:

$$\Gamma(F) = \left(\frac{2\pi t}{f}\right) \frac{F(\omega^2)}{A} \tag{9}$$

where:

$F(\omega^2)$ = force due to centripetal acceleration

A = area of photoelastic material loaded with a proof mass

The force the proof mass exerts on the photoelastic material with rotation rate is found to be:

$$F(\omega^2) = 4\pi^2 R\omega^2 \tag{10}$$

where:

R = radial distance from center of rotation

m = proof mass

ω^2 = angular rotation rate (rev/sec)

6

The area of the photoelastic material subjected to loading is:

$$A = t \times w \tag{11}$$

where:

    t = optical thickness of photoelastic material

    w = photoelastic material width

Substituting equation (10) and equation (11) into equation (9) yields:

$$\Gamma(\omega^2) = \left(\frac{8\pi^3 Rm}{fw}\right)\omega^2 \tag{12}$$

Equation (12) shows that the rotation rate induced birefringence is dependent on the width of the photoelastic material (w), the photoelastic material (f), the proof mass (m), and the distance *from* the center of rotation that the proof mass is located (R). Equation (12) also shows that the sensitivity of a fiber optic rotation rate sensor for a given configuration can be adjusted by varying the width of the photoelastic sensing element.

For a rate sensing application, the sensor output is linear with the square of the rotation rate. This results in an increased rate in either direction inducing a positive change in birefringence. It is desirable to optically bias the system to exploit the maximum linear sensing range by adding birefringence, in the form of a fixed wave plate. Incorporating this requirement into Equations (1) and (2) gives:

$$I_{-\pi/4} = I_o \left(1/2 - 1/2(\cos(\Gamma(\omega^2) + \Gamma(wp)))\right) \tag{13}$$

$$I_{+\pi/4} = I_o \left(1/2 - 1/2(\cos(\Gamma(\omega^2) + \Gamma(wp)-\pi))\right)$$

$$= I_o \left(1/2 + 1/2(\cos(\Gamma(\omega^2) + \Gamma(wp)))\right) \tag{14}$$

7

where:

$\Gamma(wp)$ = fixed birefringence from a waveplate

In order to gain insensitivity to the effects of source light intensity variations, the sum-difference sensor output detection scheme is utilized. Re-expressing equation (8) with equations (13) and (14) yields:

$$\text{sum-difference} = \cos\,(\Gamma(\omega^2) + \Gamma(wp)) \tag{15}$$

Hence, the sum-difference sensor output depends only on the angular rotation induced birefringence and the fixed birefringence introduced by the waveplate.

As equation (15) suggests, the sum-difference output varies between -1 and +1 with birefringence. The linear range of this relationship extends between -.6 and +.6. In the roll rate sensor, an increase in the angular rotation rate (either positive or negative) always results in an increase in the angular rotation induced birefringence. Consequently, for this application it is desired to optically bias the system such that for 0 rotation rate, the sum-difference output is -.6. For an angular rotation rate of ±6 rev/s, the sum-difference output should be .6. In order to accomplish this $\Gamma(wp)$ is chosen to be 4.07 radians. This results in the sum-difference output having a value of -.6 with 0 rotation rate. With an increase in the angular rotation rate, the sum-difference output will now increase. The parameters t, R, m, f and A in equation (12) are now chosen such that for ω = 6 rev/sec, $\Gamma(\omega^2)$ = 1.2. The technique described above can be used to design rotation rate sensors with different measurement ranges and sensitivities.

8

The roll rate sensor in a launch environment will be subject to many forces other than radial acceleration. These forces should act uniformly on any and all sensors in a projectile. Since the roll rate sensors are sensitive only to the radial components of these forces, averaging outputs from two opposing sensors will allow the non-rotation induced radial force components to cancel.

Computer Programs

Several computer programs were generated over the course of the contract in order to model the effects of parameter changes on sensor response, to determine the fringe constant and mechanical loads in photoelastic materials, and to acquire and compare experimental data. The MathCAD document included in Appendix B uses the relationships presented in the previous section to model the effects of parameter changes and plots sum-difference response versus rate. Some models were written in BASIC or C to isolate a given parameter or generate data files, but share the same basic algorithm. Other programs were written to control data acquisition for a given experimental configuration.

One of the first studies examined the effect of loading on the sensing elements to ensure that the photoelastic material's mechanical properties were sufficient. Figure 3 shows the force generated by various proof masses as a function of rate. Division of the force by the cross-sectional area of the sensing element results in the loading incident on the element. The loading must remain within the yield strength for the sensing material. Typical yield strengths for polycarbonates such as PSM-1 are 9×10^3 psi, quite sufficient for this application.

EXPERIMENTAL RESULTS

The first 12 months of development were used to define, procure, and assemble the necessary test equipment and instrumentation, then parameterize and optimize components in a sensor test bed. Computer models to predict material loading and sensor outputs were used to study design tradeoffs and evaluate sensor performance. Initial testing was performed on a sensor test bed designed to allow easy modification of sensor parameters. Use of a sensor test bed allowed testing of a variety of photoelastic materials and geometries, under and assortment of loading conditions. The desired results from this testing were optimal designs for sensor geometry, and defined methods of mounting and loading the sensing element. This data was then used to design a prototype MRRS. Several prototype sensors were constructed for rate table testing at ARDEC, Picatinny Arsenal. The design of these sensors was also constrained by the mission specifications of the Copperhead guided munition as defined in Appendix A. Evaluations of the MRRS were performed during two separate tests at ARDEC, in May and July of 1989. Rate tests were performed on four sensors during each two day session.

Laboratory Setup

The experimental setup at GEO-CENTERS consists of a rate table system and data acquisition/analysis instrumentation. An initial task in the project was to determine the testing and instrumentation requirements for sensor evaluation. An integral part of the testing effort incorporates a rate table to subject the sensor to the anticipated rotational forces (up to 6 rev/sec or 2200 deg/sec). The cost of purchasing a commercial rate table was prohibitive; therefore, a suitable system was constructed in-house.

The rate table system consists of a 12-1/2" diameter plate driven by a variable speed (0-2500 rpm) DC motor through a 5:1 gear reducer, and coupled to the plate by a belt drive. Plate speed is monitored by an optical shaft encoder connected to a digital counter. Eighteen signal lines run from the plate to a front panel via slip rings. The rate table system allows sensors to be evaluated for rotation rates of 0-500 rpm (0-8.3 rev/sec or 0-3000 deg/sec).

The instrumentation for collection of data from the rate table consists of a Tektronix 11401 Digitizing Oscilloscope (Tek 11401) connected to a Compaq Portable II Personal Computer (PC). Rate table speed is monitored by a counter/time to allow acquisition of data points at known rates. Digital data is acquired and downloaded from the Tek 11401 under control of the PC. The data is low pass filtered at the inputs to the Tek 11401 to remove motor control noise.

The experimental setup has been assembled to allow flexibility in both experimental procedure and change of sensor parameters. Data is stored directly on the PC from the digital oscilloscope allowing immediate calculation and plotting of difference/sum data. Comparison with computer generated models is readily performed. An overview of the experimental setup is shown in Figure 4.

Experimental Approach

A pair of identical sensor test beds for parameter studies were designed and constructed out of aluminum. The overall size is 2" x 2" x 4"; this is much larger than a sensor prototype. The larger size was chosen for the initial development phase to provide easy access during changes and adjustments of all sensor

11

components. A cutaway view of the roll rate sensor test bed is shown in Figure 5, viewed looking down at the rate table. The test bed features are discussed in the following paragraphs.

The source and detector mounts are adjustable in the Z direction to allow for optical alignment. A threaded bushing contains the collimating lens, with a locknut to fix it in position at the correct position. After a particular source is collimated, an aperture is fixed to the end of the bushing to provide a circular beam approximately 1 mm in diameter.

The polarizer and wave plate are installed in slots in the sensor test bed. The photoelastic sensing elements are installed on a removable stage to allow quick changes and alignment of elements. The beamsplitter/prism/polarizer assembly is fastened into a positioning recess in the sensor test bed.

The proof mass consists of a solid cylinder with holes bored in it. This allows the mass to be varied by the addition of high mass (Tungsten) slugs. The proof mass slides in a bushing that is press fit into the cover of the sensor test bed. Air passages are incorporated to prevent damping of motion. The proof mass and bushing are machined as a matched set and sets have been made from aluminum, teflon, and oilite (bronze impregnated with oil).

A laser diode is used as the optical source for the sensor. The laser diode contains a detector in the same package; this provides a feedback signal to the laser diode current drive circuitry. Once the drive current is adjusted for a given laser diode, constant optical output power is maintained by the drive circuitry.

A photodetector bi-cell is used for optical signal detection. Two detector circuits are necessary, one for each detector in the bi-cell. The circuits used initially consisted of a detector buffer amplifier followed by a variable gain stage for each channel. Later versions incorporated fixed gain stages optimized for the detectors used in the prototype MRRS, which also included limited frequency response and a 50Ω output to limit noise. The schematics for the final version are shown in Appendix C.

An apparatus for determining the fringe constant of individual photoelastic sensing elements is also utilized. This setup has aided the comparison of experimental data with computer generated models. The apparatus uses the prototype sensor or test bed with no proof mass. A known weight is applied to the sensing element through the use of a lever arm. Maxima and minima for each optical channel is recorded, along with the weight at those points. This information along with the dimensions of the sensing element and lever arm can be used to calculate the fringe constant for the given element. This setup is shown in the photograph of Figure 6.

A number of preliminary experiments were performed to examine the effects of sensing element geometry on sensitivity. The sensitivity is inversely proportional to the width of the photoelastic material in contact with the proof mass; for mounting purposes, a large base was desirable. A number of shapes cut from the same material (PS-2A) were examined. The shapes ranged from triangular to inverted "T".

The inverted "T" geometry was initially chosen as the preferred photoelastic material geometry for the sensing element. A test matrix of photoelastic materials and dimensions was

13

generated to evaluate in the sensor test bed. The matrix is shown in Table 1 with the measured dimensions of the samples tested.

Preparation of the sensor test bed for parameter evaluation consists of the following steps. A sensing element machined from a piece of sheet stock is visually examined through crossed polarizers. Any residual birefringence (seen as colored bands through polarizers) from machining requires that the piece be annealed. The annealing process soaks the material at a temperature close to the softening point to remove any machining induced strain in the material.

The sensing element is then placed in the holder and positioned in the sensor test bed. Optical alignment is checked to ensure the collimated beam passes through all optical components correctly. The sensor electronics are then calibrated by manually loading the sensing element with a known mass to determine the maximum and minimum detector outputs for each channel. Offset and gain settings are adjusted to provide identical offsets and peak to peak outputs for the two detectors (this occurs as the sensor output polarization cycles through maximum and minimum intensities). If the unloaded output of the sensor is near a max-min point, the waveplate is changed to optically bias the system at a different point. The unloaded outputs, max-min outputs, and respective loads are recorded for later calculation of the difference/sum output and material fringe constant. A photograph of the disassembled sensor test bed is shown in Figure 7.

After calibration, the sensor test bed is assembled with the desired proof mass and bushing installed in the cover as shown in Figure 8. The sensor test bed is then clamped into position on the

14

rate table platter and connected to the electronics, as shown in Figure 9. Output data from the sensor is acquired starting at 8.0 rev/sec (2880 deg/sec). The rate is decreased in steps of 0.4 rev/sec (144 deg/sec) down to 4.0 rev/sec (1440 deg/sec). The rate is then decreased to 0.1 rev/sec (36 deg/sec) in steps of 0.1 rev/sec. At this point the rate is increased following the same incremental pattern. This allows observation of any hysteresis present in the sensor.

Initially, a total of 77 test bed data sets were generated covering 40 different sensor configurations. These sensor configurations incorporated the candidate materials from Table 1 with several different proof masses, and define the initial test matrix. The initial experiments were performed with a teflon proof mass and bushing. However, a change in the sensor output at sustained high (8.0 rev/sec) rates raised suspicion that the teflon proof mass was deforming under load. For this reason, an aluminum proof mass/ sleeve assembly was constructed for generating the data sets shown in Table II.

The most sensitive configuration tested from Table II used the smallest sensing element (.040" x .040" nominal) of PSM-1, and the maximum proof mass (31.66 g). This configuration resulted in the sensor output cycling through a fringe during loading. The individual detector outputs are shown in Figure 10 for a test using this configuration. The increase in optical transmission for one polarization and corresponding decrease for the orthogonal polarization can be seen as a function of rate. These outputs are voltage levels from the detector amplifiers that have been sampled as previously described. The difference/sum algorithm uses these

15

voltage data as input, and produces the normalized output data shown in Figure 11. The output predicted by the model is also shown.

Initial output data recorded the difference/sum output versus rate calculated by the digital oscilloscope. During the data collection, it was realized that the offsets from calibration data were necessary in the difference/sum calculation to normalize the sensor output. From that point on, the recorded data consisted of the individual sensor outputs, and the rotation rate. The difference/sum calculation was performed following a given test.

The output shown in Figure 11 is normalized and will vary between ±1. The sensor output cycles through a maxima. Additionally, the output is now independent of variations in source intensity, and gain and offset differences in the detector amplifiers.

A sensor configuration that results in its output increasing through a maxima was often used to evaluate sensor performance. In this case it is easier to compare the model to the sensor output (by comparing the rate at which maxima occur). The operating range in a working roll rate sensor will only make use of outputs between ±0.6, where the response is approximately linear. The linear region between ±0.6 can be easily seen when the output is viewed versus rate squared, as in Figure 12. The generation of the data base from the matrix of Table II has shown that the linear range of sensor response can be tailored to operate over a variety of rotation rates.

16

For a given radial position and sensing element material, sensor response is determined by the width of the sensing element and the proof mass. Decreasing the proof mass will decrease the sensor sensitivity to angular rate because the amount of generated force is decreased. Increasing the width of the photoelastic sensing element will also decrease the sensitivity, because the force is distributed over a larger area resulting in less induced birefringence. The optical thickness has no effect on the induced birefringence in this sensor (see Equation 12), and thus no effect on the sensitivity.

Figure 13 shows sensor test bed response utilizing a wider sensing element (.080" nominal) for a variety of optical path thicknesses (.040", .125", and .250" nominal), and a proof mass of 20.65g. The responses are all similar. Differences can be attributed to sensing element variations from the nominal width, residual birefringence (not eliminated by annealing) in the sensing element causing an optical bias, and not including detector offset when calculating the difference/sum output. Increasing optical path thickness can increase the yield strength of the sensing element without affecting sensitivity. However, the increased thickness on the typically narrow sensing elements may result in torque-induced birefringence affecting sensor response. In addition, optical alignment becomes more critical when the beam must pass through a long narrow sensing element. One sensing element with an optical thickness of 0.375" was examined. The annealing process had not removed all the residual birefringence, and because of the inhomogeneities in its optical properties, it was shown useless as a sensing element. For these reasons, sensing elements with reasonably short optical path lengths ($\leq$.125") are preferred.

17

Another method to alter sensor sensitivity is through the choice of photoelastic materials. Another plastic, PS-2A polycarbonate, was also evaluated. This material is a slightly stronger plastic, but is less sensitive than PSM-1 polycarbonate material. It also darkens considerably during the annealing process. Sensor test bed data for this material is shown in Figure 14, along with the predicted response. For the application of projectile roll rate sensing, PSM-1 was the prime photo-elastic material choice.

Hysteresis is present in the data shown in Figures 13 and 14. It is known from GEO-CENTERS, INC. work with other types of birefringent sensors that hysteresis is not inherent to these photoelastic materials. The hysteresis is mechanical in nature and has been attributed to several factors. Most of the test bed experiments performed subsequent to generating the data base has been an attempt to isolate causes of hysteresis.

The only cause of hysteresis involving the sensing element is the method of mounting. This became evident when bonding the inverted "T" sensing elements to the sensor test bed holders. When the elements were bonded with epoxy along the base, the epoxy would occasionally have a bubble or delaminate resulting in a yield point. Careful bonding with fillets on the two ends of the element gave the most consistent results and the least hysteresis.

Care must also be taken that the sensing element has no contact with any surfaces during loading. One of the sensing elements had warped slightly from the annealing process, and gave erratic results due to non-axial loading. During efforts to prevent bending of the element, small braces were placed on the front and pack sides. At first these caused severe hysteresis from

18

contact with the sensing element, but results were much improved by the use of a single, appropriately placed brace. However, bracing is not a satisfactory solution and is not used in the prototype device.

The active sensing element area is only where the optical beam passes through the photoelastic material. For a sensing element of uniform rectangular (x-y) cross section, the point in the z-axis at which the beam passes through the material will be unimportant. One of the difficulties in machining the inverted "T" geometry was maintaining a uniform cross-section because of chipping and material movement during the machining process. To solve this problem, a different element geometry was tested; simply a post with a rectangular cross-section. There is no base as in the inverted "T" geometry, so during machining the piece can be supported by a jig on all sides except the side being machined. This prevents movement of the piece and has resulted in much better tolerances. It also has provided superior quality of the loading surfaces. Several photoelastic sensing element machined with this technique have not required annealing because there was no machining induced birefringence caused with elements fabricated in the jig. Data acquired with this type of sensing element has provided the best test bed results, as can be seen from Run 88 in Figure 15.

Run 88 used a aluminum proof mass lubricated with a teflon spray on the bushing to reduce friction. Another test was performed with the sensor untouched from Run 88 to examine repeatability. The results of this are shown in Figure 16, where runs 88 and 89 are plotted together. The two responses track each other well. The sensor was allowed to sit for 48 hours, and then a test run was

19

repeated. Results from this test shown in Figure 17 do not track the previous data. After sitting unused on the rate table for two days, the sensor output exhibited a large amount of hysteresis. This could be due to the teflon lubricant coagulating, or the proof mass settling on a slight angle inside the bushing. However, there remains a problem of hysteresis due to restriction of movement of the proof mass in the bushing.

Hysteresis has been demonstrated to be associated with mechanical effects in the sensor test bed. Experiments identical to those discussed above have shown the output to be independent of whether the sensor test bed had been recently reassembled. Experimental data exhibiting hysteresis upon test bed reassembly have shown a lack of hysteresis during subsequent experiments. As part of experimental procedure, the sensor test bed is calibrated before and after reassembly. Calibrations are performed by loading the sensing element directly (not with a proof mass) and have shown no change in sensor sensitivity before and after reassembly of the test bed. Therefore, hysteresis must be caused by mechanical effects associated with the acceleration induced loading of the sensing element.

Several mechanical effects associated with the proof mass cause occasional hysteresis in the data. Early on in the testing, it was discovered that motion of the proof mass had been damped by "stiction". Air passages solved this first problem. A second source of hysteresis is due to static and dynamic friction, and tolerances that allow the proof mass to get slightly canted in the bushing. A redesign of the proof mass was built incorporating a tool steel shaft and brass proof mass with .0005" clearance to reduce friction and wobble, with air passages also included. This

design resulted in a marked improvement as shown by the data in Run 172 in Figure 18. Based on the experience gained with roll rate sensor test bed, design commenced on the prototype MRRS.

MRRS Prototype Design

The Copperhead mission specifications and the design constraints learned from the sensor test bed experiments led to the design of the prototype MRRS. Loading of the sensing element must utilize mechanical designs that minimize both static and dynamic friction forces, and restrict the motion of the proof mass to a single-axis. The proof mass will probably be the largest single component in the sensor; choice of its material must be optimized for high density, low friction, and small deformation properties. The sensing element must be supported and shaped in such a way as to provide uniform strain and maximum sensitivity at the point of optical access. Selection of appropriately matched optical components is necessary to maximize sensitivity. Optimization of these material and mechanical properties will yield a roll rate sensor with the designed operational characteristics.

Several mechanical designs for loading the sensing element with a proof mass were considered and discussed between ARDEC and GEO-CENTERS. The sliding proof mass was replaced by a proof mass mounted on a hinged carrier to be less susceptible to launch shocks. The carrier incorporates a guide for the sensing element to insure orthogonal loading. Because the actual movement required by the compression loading of the sensing element is only a few thousandths of an inch, the prototype sensor housing was designed with small clearances in order to support the proof mass/carrier

combination under severe loads. This prevents plastic deformation of any components, and limits the maximum load to the sensing element under launch conditions.

To accommodate the size constraints for the Copperhead munition, the optical path was folded using a mirrored right angle prism and a cube beamsplitter, as shown in Figure 19. The size constraints were relaxed slightly to allow use of off-the-shelf electro-optic components and bulk optics, as these components can be obtained with reasonable cost as production items in reduced size. Folding of the optical path also allows the electrical connections to all occur in the same local area of the sensor. This can be seen in the top view of a partially assembled prototype sensor shown in Figure 20.

The mechanical components are shown listed with their drawing reference numbers in Figure 21. Referring to the figure, the proof mass (4) is simply a block of high density machinable tungsten. The proof mass carrier (1) contains a rectangular hole to accommodate and guide the sensing element (not shown). When assembled, the rectangular hole is covered by the proof mass which provides the loading surface to one end of the sensing element. The carrier also has provisions for mounting a waveplate on either side of the sensing element broach through which optical access occurs. The base plate (2) has mounting fixtures for the bulk optics and, along with the optics fixture (5), provides support for the proof mass/carrier during launch. The optics fixture provides mounting fixtures for the GRIN lens, polarizer, and aperture, along with one of the PIN detectors. The other PIN detector is mounted in one of the side covers (6). The top plate (8) has adjustment screws which can be used to remove any play in the motion of the proof mass. A photograph of an assembled prototype sensor with no electro-optic components installed is shown in Figure 22.

22

As discussed earlier, the sensing range of this type of sensor can be easily adjusted by changing the proof mass and/or the sensing element width. Proof mass blanks were made to allow a maximum of approximately 50 gram mass; to obtain a smaller mass some of these had material removed from the top and/or sides. The proof mass is adhered to the carrier with epoxy on two sides.

The sensing element must be carefully made, as evidenced by the early experiments with different geometries. The post type of element is used in the prototype MRRS, with alignment maintained by the rectangular hole in the carrier. Several posts were machined from PSM-1 sheet stock in three nominal widths: 1, 1.5, and 2 mm. These were cut overlong, and the best pieces selected and annealed to remove any residual birefringence. The ends of these elements were then polished in an optical polishing jig through successively finer grits to provide highly square, parallel faces to act as the loading surfaces. For the second set of tests at ARDEC, additional sensing elements were fabricated out of PSM-1 by an optical fabrication job shop. The dimensions of each sensing element were individually recorded and noted with the particular proof mass and sensor during assembly. No adhesives are necessary on the sensing element, as it is sandwiched between the base plate and the proof mass. Fabrication of the sensing element is an extremely labor intensive process, but it should be noted that tight tolerance sensing elements can easily be manufactured in quantity through molding processes.

MRRS Prototype Evaluations

Prior to prototype MRRS evaluations, the rate table at GEO-CENTERS was modified to use the same type of connectors as the Contravis rate table at ARDEC. This allows the testing of

23

identical sensor/electronics combinations at both facilities. An adapter plate was fabricated to mount a pair of sensors and electronics which could be mounted on either rate table platter. An interface box was also fabricated allowing connection of GEO-CENTERS data acquisition equipment to the Contravis table connectors. The sensors are actually mounted inside fixtures with sockets that bolt up to the adapter plate. A photograph of the adapter plate, electronics, and two sensors mounted on the GEO-CENTERS rate table is shown in Figure 23.

Initially four prototype sensors were fabricated for testing at ARDEC. All four sensors had a 50 gram proof mass, two with 1.9 mm sensing elements, and two with 1.3 mm sensing elements. The sensing elements were slightly thicker than originally specified because of stock tolerance specs. This required modification of the proof mass carriers to accommodate the thicker elements. This was performed by hand, grinding material from the inside of the square hole. Initial rate table testing at GEO-CENTERS gave the desired results as indicated by Run 177 in Figure 24. This sensor has a proof mass of 51g and a 1.86 mm wide sensing element. Rate testing began at 8 rev/sec, decreased to 0.1 rev/sec, then increased back up to 8 rev/sec.

Each prototype sensor was mounted in a sensor housing which allowed the sensor to be attached at a known radius and connected to a sensor electronics circuit board. The board was fitted with connectors compatible with those on the Contravis rate table at ARDEC. The sensor electronics for all sensors were identical in the gain stages, and each laser diode driver was individually adjusted for use with the laser in the associated sensor.

24

The initial tests at ARDEC evaluated the four MRRS on a more stable rate table than that available at GEO-CENTERS. Due to time constraints, only one evaluation test was performed on each pair of sensors. These initial tests showed marginal results in that a large amount of hysteresis was present in the first pair of sensors, and one of the second pair sensors failed, as it showed a constant output for all rates. This was identified as an electronics problem instead of a sensor problem. The last sensor had a small amount of hysteresis, but did not register any change in rate until about 700 deg/sec.

After the ARDEC tests, the sensors were disassembled and calibrated. All the sensors performed properly, and although there was some hysteresis present, it was not as much as seen at ARDEC. Close examination of the fit between the sensing elements and the proof mass carriers showed that the tolerances were poor and that the sensing elements were binding. This was a result of the hand fitting process used in sensor preparation. On two of the sensors, the sensing element in the carrier was tight enough to act as a tiny spring, causing non-axial loading. This lack of clearance was the cause of hysteresis. The ideal solution to this problem was to optically polish the sensing elements down to the originally specified size.

To improve the fit and clearance of the sensing element/ carrier interface, an optical polishing shop was located to fabricate new sensing elements from PSM-1 stock. This shop is capable of fabricating sensing elements to tighter tolerances than is GEO-CENTERS. Some problems were encountered with residual birefringence in the sensing element. Subsequent annealing caused the sensing element to warp. This led to the requirement that the

photoelastic sensing element be annealed prior to the final polishing of the sensing element. Two pieces were fabricated that were of sufficiently good quality to use in the prototype sensors. In preparation for the next set of tests at ARDEC, two of the sensors (2 and 4) were reassembled with these new sensing elements.

On another of the original sensors (Sensor 4), one of the sensing elements was shorter than the others, and bottomed out under severe loads. This was indicated in the data by a sudden flattening of the sensor response curve. This data proved to be beneficial and demonstrates that the design of the prototype MRRS will protect the sensing element from loading past the point of permanent deformation of the sensing element.

Further rate testing on the table at GEO-CENTERS confirmed the fact that no sensor indicated a response below about 700 deg/sec. In fact, this is also indicated in the first early data that was presented in Figure 24. Further analysis of the prototype MRRS showed that this is the correct output for the device when it is not in free flight. This can be explained by the following.

When the MRRS is spinning on a earth mounted rate table, the force of gravity is acting on the proof mass and countered by the rate table plate. Examining the moments about the hinge (or pivot) point of the proof mass carrier shows that there is a component of force acting in the opposite direction of the rate induced centripetal acceleration. This component is a function of the mass and the location of the center of gravity of the proof mass in relation to the hinge. It is defined by the force of gravity times the radial component of distance between the center of gravity and

26

the hinge, times the mass. When the centripetal acceleration due to rotation is sufficient to overcome this opposing radial component, the sensing element begins to be loaded by the proof mass.

Calculations indicate that this component due to gravity will be overcome at a rate of approximately 650 deg/sec. Experimental verification was provided by slightly changing the radial location of the center of gravity and thus the rate at which the sensor begins to respond. This was accomplished by tilting the sensor a few degrees. (This also affects the amount of radial acceleration acting on the proof mass, but the effect is negligible at small angles.) Comparison of experiments with different angles showed a corresponding shift in the onset of sensor response.

The next set of tests at ARDEC were also scheduled to test two pairs of sensors. Two sensors from the first set of tests (Sensors 1 and 3) were reassembled but otherwise unchanged. Since the clearances were unchanged from the last test, some hysteresis was to be expected. Sensors 2 and 4 were modified with new proof mass carriers and the new sensing elements. The proof mass of both sensors was nominally 50 grams. The sensing elements were 2.02 mm and 2.04 mm in width, respectively. Calibrations were performed on all the sensors for comparison against their predicted response. The sensors were loaded with weights through a maxima and minima during the calibrations. A typical calibration plot for Sensor 2 is shown plotted with the model data in Figure 25. The conditions used in the model are shown to the right of the graph, where w = width of the sensing element, wp = waveplate retardance, pm = proof mass, Γwp is the calculated birefringence of the waveplate, and f = fringe constant of PSM-1 photoelastic plastic.

Testing at ARDEC was performed to evaluate rate response and sensor stability at a fixed rate over a long period of time. The sensors were again mounted in pairs on the rate table and data collected from both at once. Stability tests were run at constant rates of 1000 deg/sec and 1500 deg/sec for various time lengths ranging from 15 minutes to 1 hour.

Figure 26 shows data from a 1000 deg/sec stability run of Sensor 1 over 1 hour. This particular data set showed the largest excursion encountered in any of the stability runs. Here a peak to peak difference/sum variation of 0.011 was observed. The variation in individual detector outputs was 5.4 mV for Detector 1 and 11.4 mV for Detector 2. Figure 27 shows a similar data set for Sensor 2 acquired at a rate of 1500 deg/sec over 1 hour. Here the peak to peak variation was only 0.0075, with variations in the individual detectors of 16 mV and 17 mV.

Rate evaluations were performed over the range from 0 to 2000 deg/sec. Both clockwise and counter-clockwise spins were used, and the MRRS proved insensitive to direction of spin as expected. Outputs for Sensors 1 and 3 are shown plotted against rate in Figure 28. These sensors should have almost identical outputs because their sensing elements are the same size and their proof masses differ by only 1.89 grams. The slight difference in the response curves are caused by this difference in proof mass. The differences in starting point for the rate output are caused by the difference in waveplate retardance in the two sensors. The hysteresis is caused by the tolerance problems previously discussed. The hysteresis is significantly less than that observed during the first tests at ARDEC.

Tests with the new sensors show significant improvement due to the new sensing elements and carrier, substantiating that clearance problems are the source of hysteresis. Figure 29 plots the results of rate tests using the new Sensors 2 and 4. Two runs are superimposed on each other for each sensor, allowing comparison of different experiments. Significant reduction in hysteresis is evident in Sensor 4, and hysteresis is virtually eliminated in Sensor 2. Also evident is the repeatability of the data between Runs 201 and 204. (Between these experiments the sensor had been removed from the test setup). The sensor response begins to occur at 650 deg/sec, as predicted by the above discussion.

Subsequent to Run 204, Sensors 2 and 4 were disassembled, and the sensing elements were flipped 180 degrees and reinstalled. This was done to examine the sensitivity of the sensor to the repositioning of the sensing element. Comparison of data acquired after reassembly showed a small amount hysteresis equivalent to that of Sensor 4 in Figure 29, and a slight shift in offset due to a change location of the optical beam through the sensing element. Sensor 4 also showed a slight change in responsivity, indicating that non-uniform loading of the sensing element was occurring. These results indicate that the operation of the MRRS is extremely dependent on the quality of the sensing element/proof mass carrier interface, and that with proper attention to precision, the desired performance can be obtained.

CONCLUSIONS AND RECOMMENDATIONS

The Phase II "Micro-Miniature Roll Rate Sensor Program" developed an optical centripetal accelerometer that can be tailored to work over a wide range of accelerations. A rate sensing device was developed by measuring centripetal acceleration due to rotation

with a proof mass loading a photoelastic sensing element. The acceleration is proportional to the amount of birefringence induced by the load. Development of this technology resulted in construction of a prototype rate sensor targeted for use with the Copperhead munition. The sensors developed in this program can be adjusted for the desired range of operation through changes in width of a photoelastic (plastic) sensing element and/or changes in the amount of proof mass used to load the sensing element. Radial location of the sensor can also be used to control the range.

The prototype devices developed in this program utilized self-contained sources and detectors. This technology also lends itself to utilization of optical fibers for transmission of raw data.

The MRRS provides an output proportional to rate squared. Because of this, it is insensitive to direction of spin. It is also more accurate at higher rates the low rates, because friction forces become proportionately larger at low rates. For use in a free falling projectile such as Copperhead, a paired sensor system was devised with sensors placed opposite the center of rotation. This allows any lateral accelerations to be canceled out through vector addition, and results in a measurement of only rotation induced radial accelerations.

The development of the MRRS resulted in a unique hinged loading scheme contained in a rugged package that allows both uniaxial loading and protection from plastic deformation of the sensing element. In an effort to develop the prototype from readily available components, size constraints were relaxed enough

to accommodate off the shelf components in the sensor housing. The total package was not tested in an airgun because of cost and scheduling constraints. However ARDEC has been evaluating individual electro-optic components of the same family in airgun shock tests. The total size of the package is sufficiently small to allow four of these devices to be installed in the area reserved for rate sensing according to the Copperhead specifications.

Associated electronics is currently contained on one circuit board per sensor, each of which contains four integrated circuits and several small components. These electronics are simple in nature and can be significantly reduced in area through the use of standard production techniques. All electronics operate off the specified available voltages.

To meet Copperhead performance specifications will require four sensors, two tailored for low rate sensitivity, and two for high rate sensitivity. Because no free flight rate testing was feasible in this Phase II program, low rate performance evaluations were not measured. Model predictions indicate that it is unlikely that the desired performance of 1 deg/sec will be achievable at rates below 200 deg/sec. However, the upper range of performance can be extended well beyond the specified 2000 deg/sec.

The evaluations of the MRRS indicate that the most recent improvements in sensing element fabrication significantly enhanced stability and accuracy of the sensor. However, this device is not an ideal implementation of a rate sensor where high accuracies are required at low rates of rotation. Because future development of the Copperhead munition is unlikely at this point, pre-production development of this sensor to the Copperhead specifications may not

be warranted. Advanced munitions currently in development require even more severe performance specifications where rate sensors are required for navigational purposes. These specifications can be better met by such optical technologies as the optical fiber gyroscopes currently in development at ARDEC.

Requirements for a simple rate sensing device for high rates of rotation (such as a deceleration fuze) or a rate switch could easily be met by the technology developed in this program. The MRRS may also provide a simple method of measuring rotation rate at the exit or a gun barrel in order to determine munition exit velocity from spin rate. Because the MRRS is an optical accelerometer, it can also be readily adapted to any accelerometer requirements. It provides a unique capability over conventional accelerometers in that in can monitor a continuous (DC) acceleration for long periods. GEO-CENTERS is actively pursuing commercial applications of the MRRS technology in these areas.

Table I.   "T" Sample Matrix

PE Material	Optical Thickness	Sensing Element Width	
PS-2A	.126"	.049,	.091
PSM-1	.045"	.043,	.080
	.120"	.044,	.078
	.229"	.045,	.085
	.369"	.050	

TABLE II. DATA BASE MATRIX FOR INITIAL EXPERIMENTS
(identified by lab book run number)

Sensing Element Parameters (measured)				Test Run Numbers — Proof Mass (grams)				
Type	Thickness in (mm)	Width in (mm)	Fringe constant psi/f/in	18.14	20.65	23.15	25.65	31.66
PSM-1	.045 (1.143)	.043 (1.092)	57	15,16,19, 77	20	21	22	17, 23, 68
		.080 (2.032)	60	10	11	12	13	14
	.120 (3.048)	.044 (1.118)	66	33	34	35	36	37
		.078 (1.981)	60	30	29	28	27	26, 31, 32
	.229 (5.817)	.045 (1.143)	67	44	45	46, 47, 48	49, 50, 51	52, 53, 54
		.085 (2.159)	59	43	42	40, 41	39	38
	.369 (9.373)	.050 (1.270)	60					69, 70, 76
FS-2A	.126 (3.200)	.049 (1.245)	88	55, 56, 57	58, 59, 60, 61	62	63	64, 65, 66, 67
		.091 (2.311)	72	75	74	73	72	71

Note: On most plots of data, a data set descriptor is given which identifies the sensing element and proof mass. The descriptor is defined as follows:

        sensing element material (0 = PSM-1, T = PS-2A)
        Nominal element thickness in 10 $^{-3}$inch
        Nominal element width (N = .040", W = .080")
        Proof mass in grams
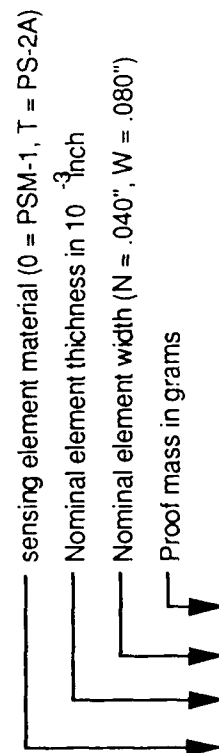
0 250 N 18

All runs with this descriptor used a 1/4" thick, narrow PSM-1 sensing element loaded by an 18 gram proof mass. Run 44 is the only test fitting this description.
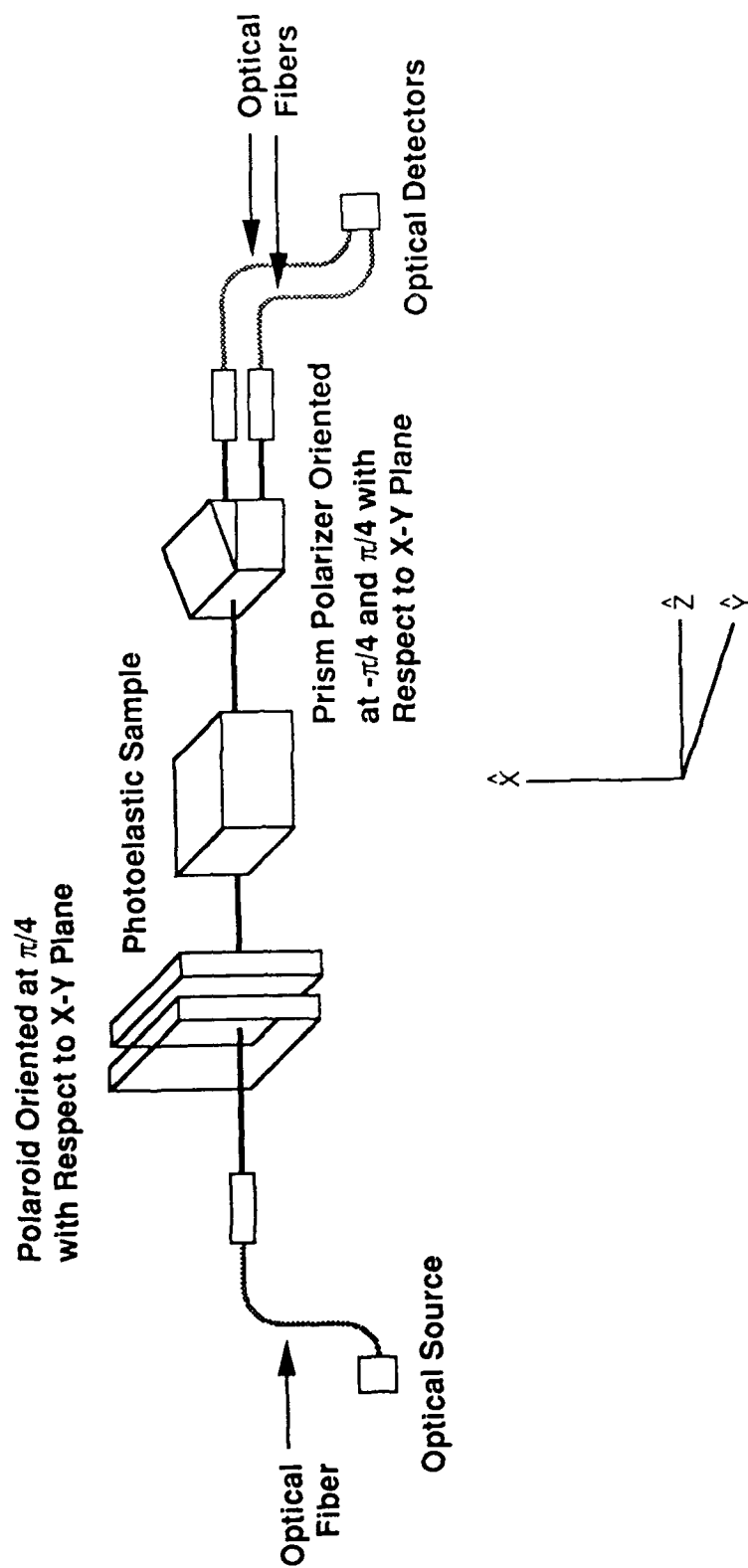
Figure 1. Schematic of the Optical Configuration of a Photoelastic Stress Sensor.
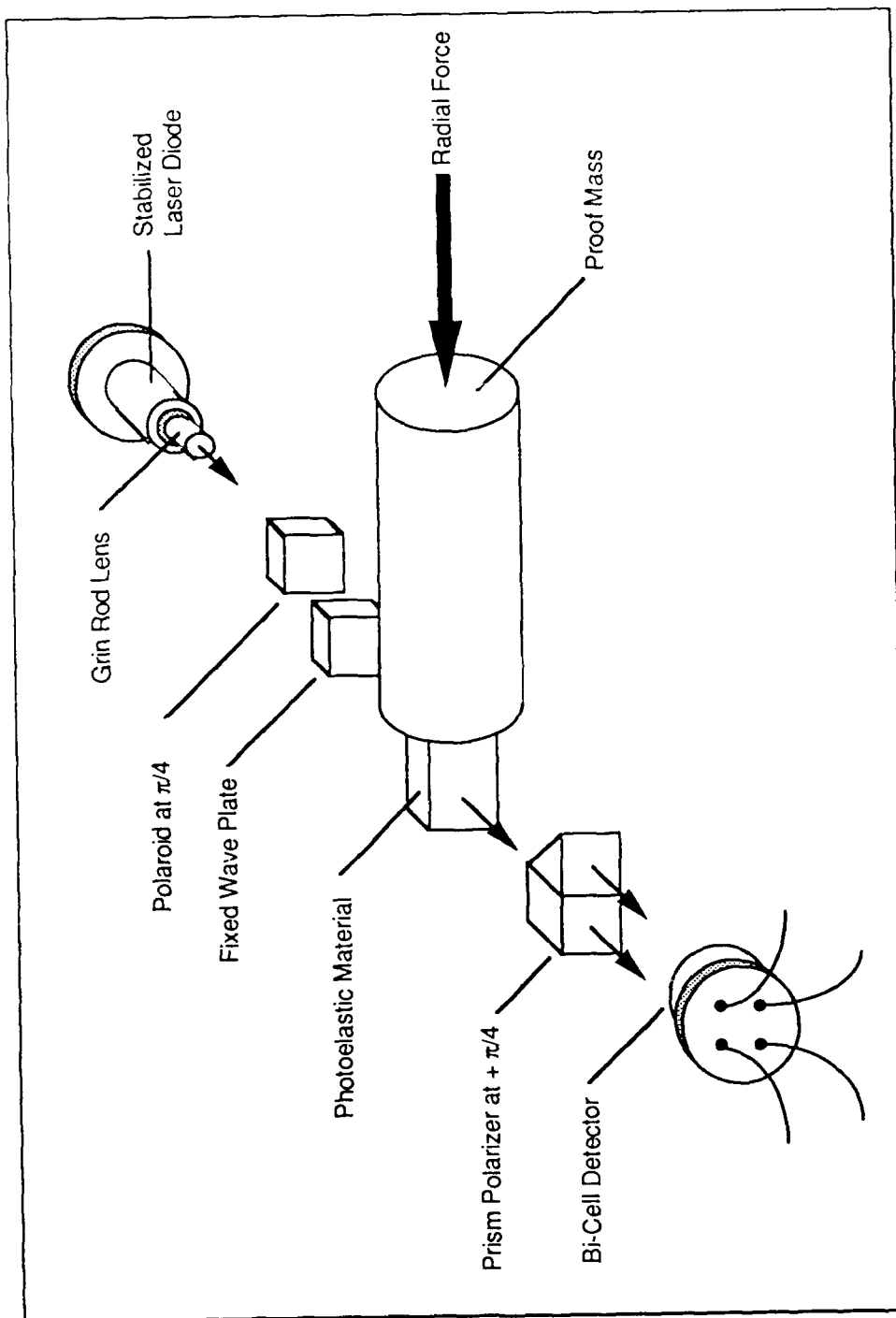
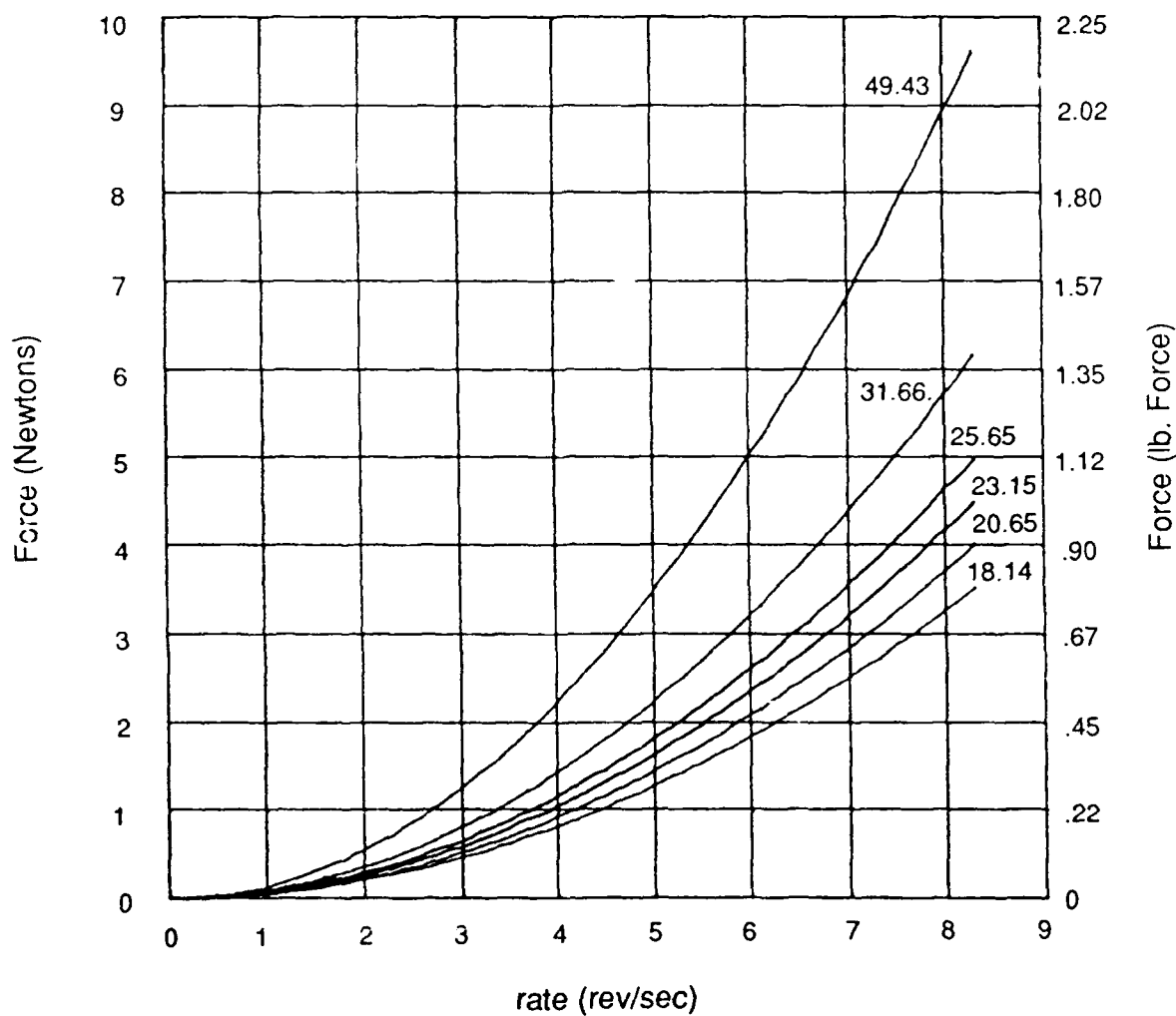Figure 2. Components and their orientation for the micro-miniature roll rate sensor test bed.

Labels in figure:
- Stabilized Laser Diode
- Grin Rod Lens
- Polaroid at $\pi/4$
- Fixed Wave Plate
- Photoelastic Material
- Prism Polarizer at $+\pi/4$
- Bi-Cell Detector
- Radial Force
- Proof Mass

Figure 3.   Force in Newtons as a function of angular velocity in
            rev/sec for a set of proof masses = (18.14, 20.65, 23.15,
            25.65, 31.66, 49.43) grams.

37
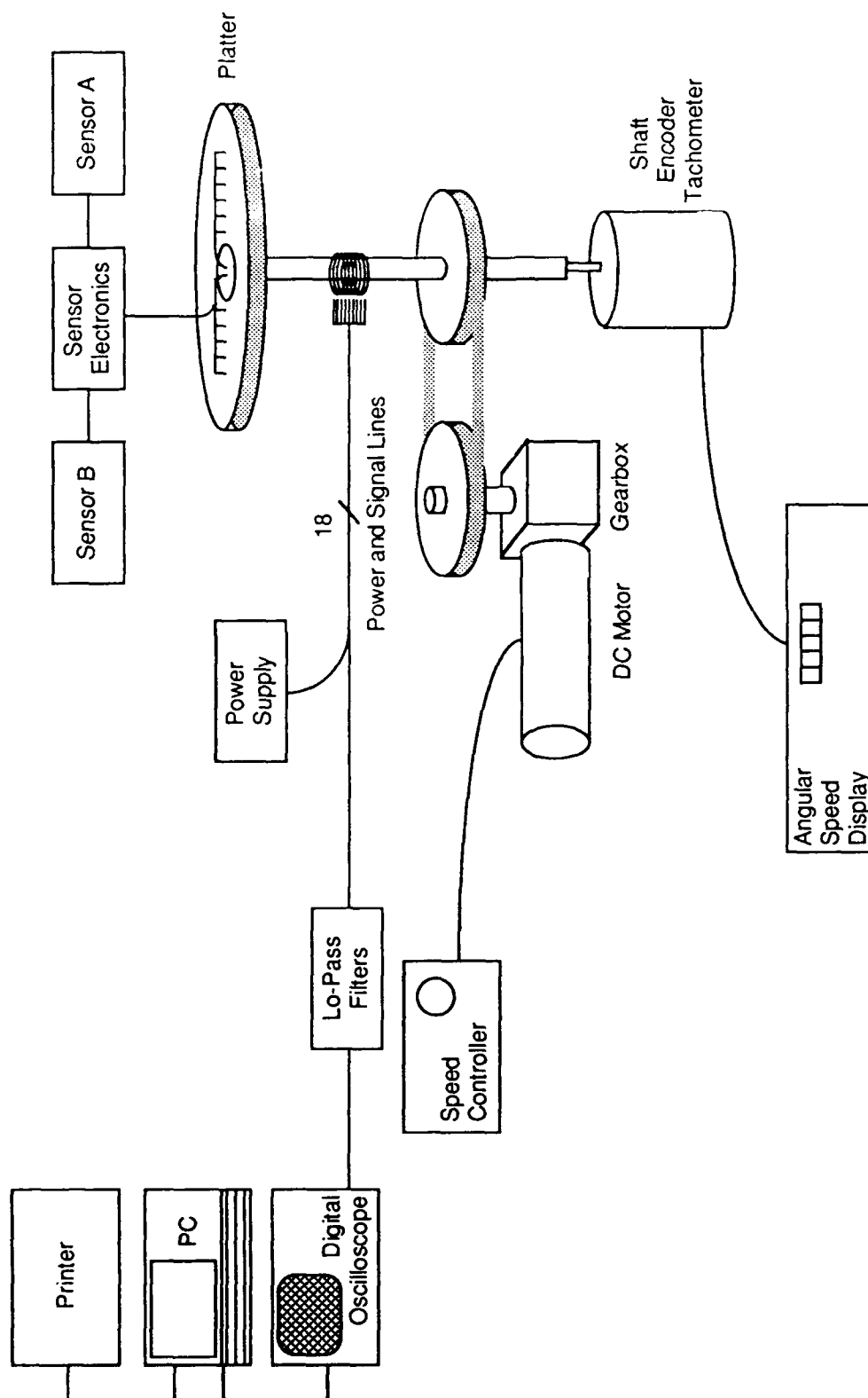
Figure 4. Laboratory Setup and Instrumentation.

38
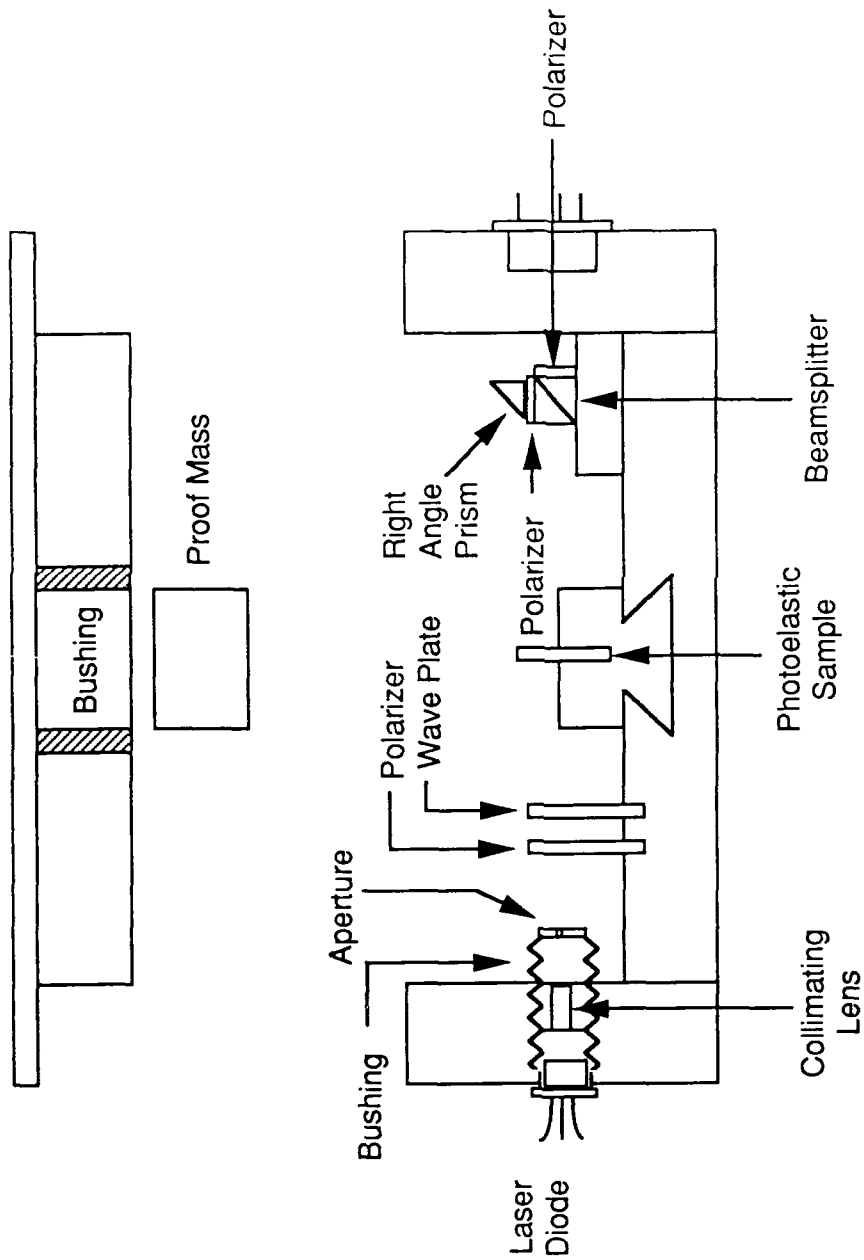
Figure 5. Cutaway view of the roll rate sensor test bed and component locations.

39
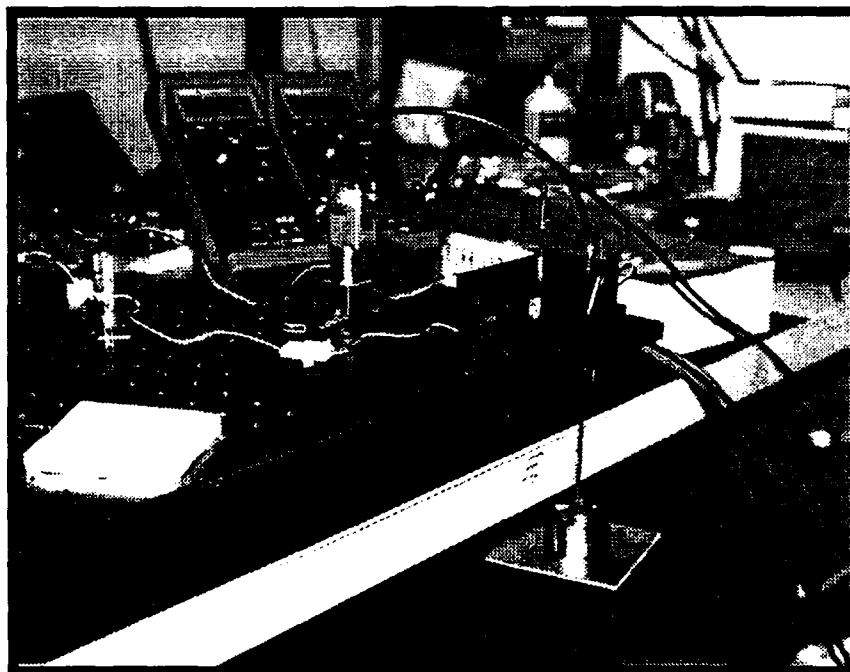
Figure 6. Apparatus used to calibrate and determine the fringe
constant for a given test bed configuration.
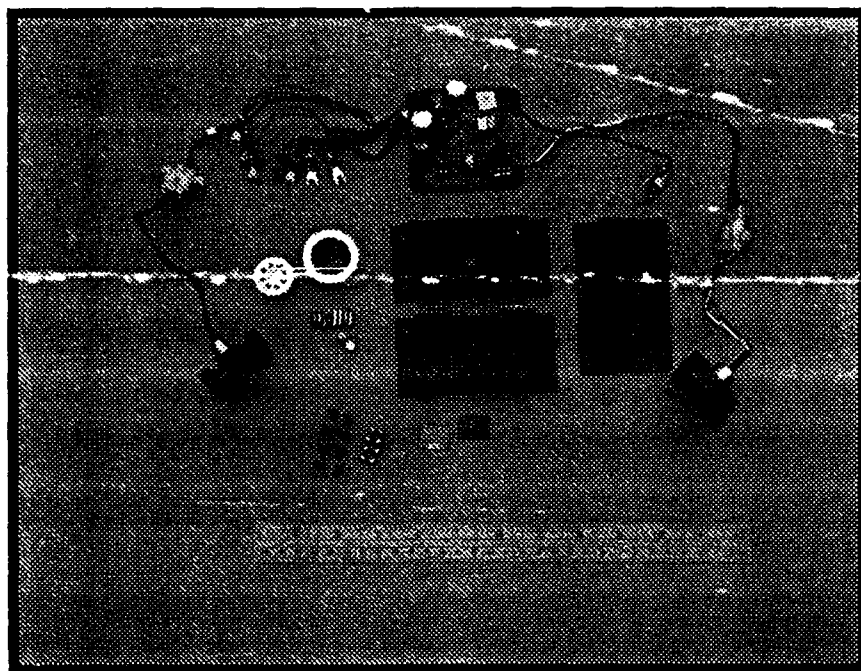
Figure 7. Photograph of the sensor test bed components and electronics.
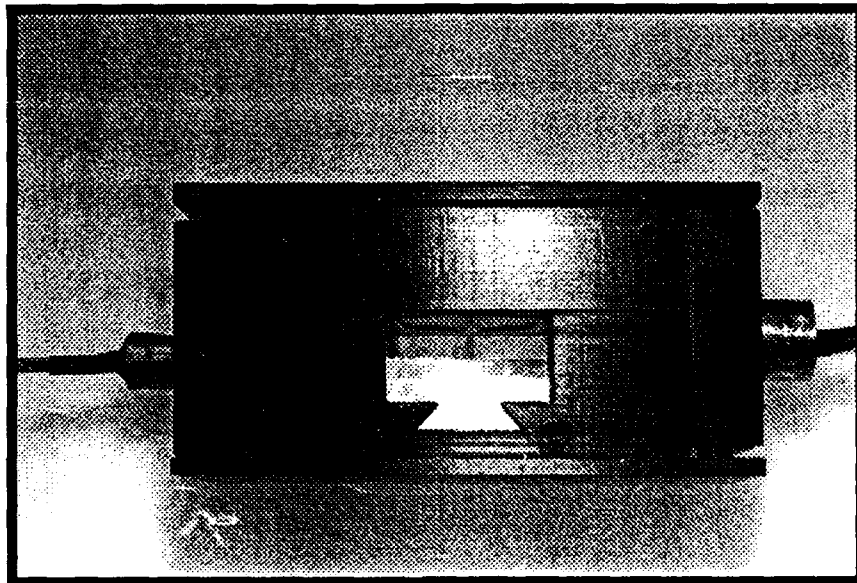
Figure 8. Assembled sensor test bed viewed with sides removed. Laser diode source is on the left, bicell detector on the right. Radial acceleration acts from the top of the page.
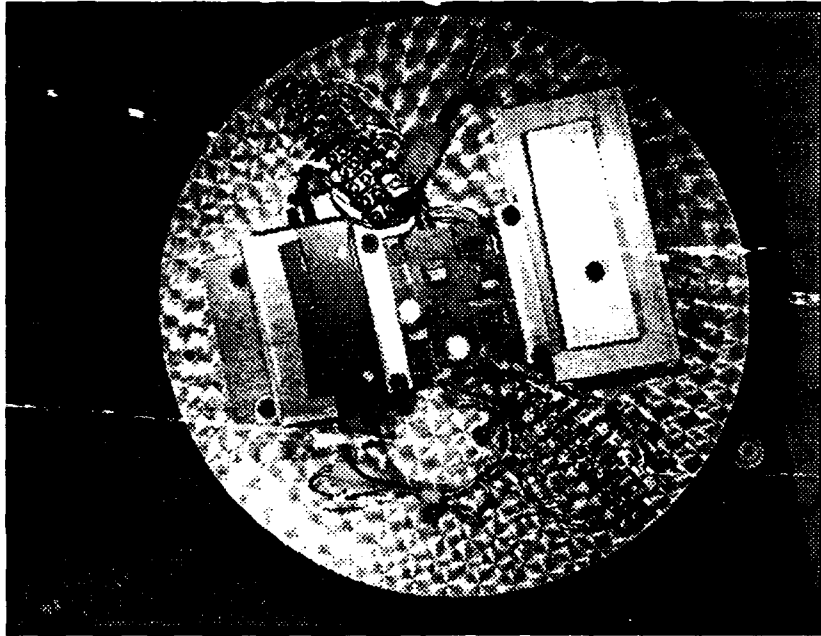
Figure 9.   View looking down on the rate table plotter.
            The sensor test bed is clamped into position
            on the left. An equal mass counter weight is
            bolted in place on the right.

42

RUN 68 3-3-68
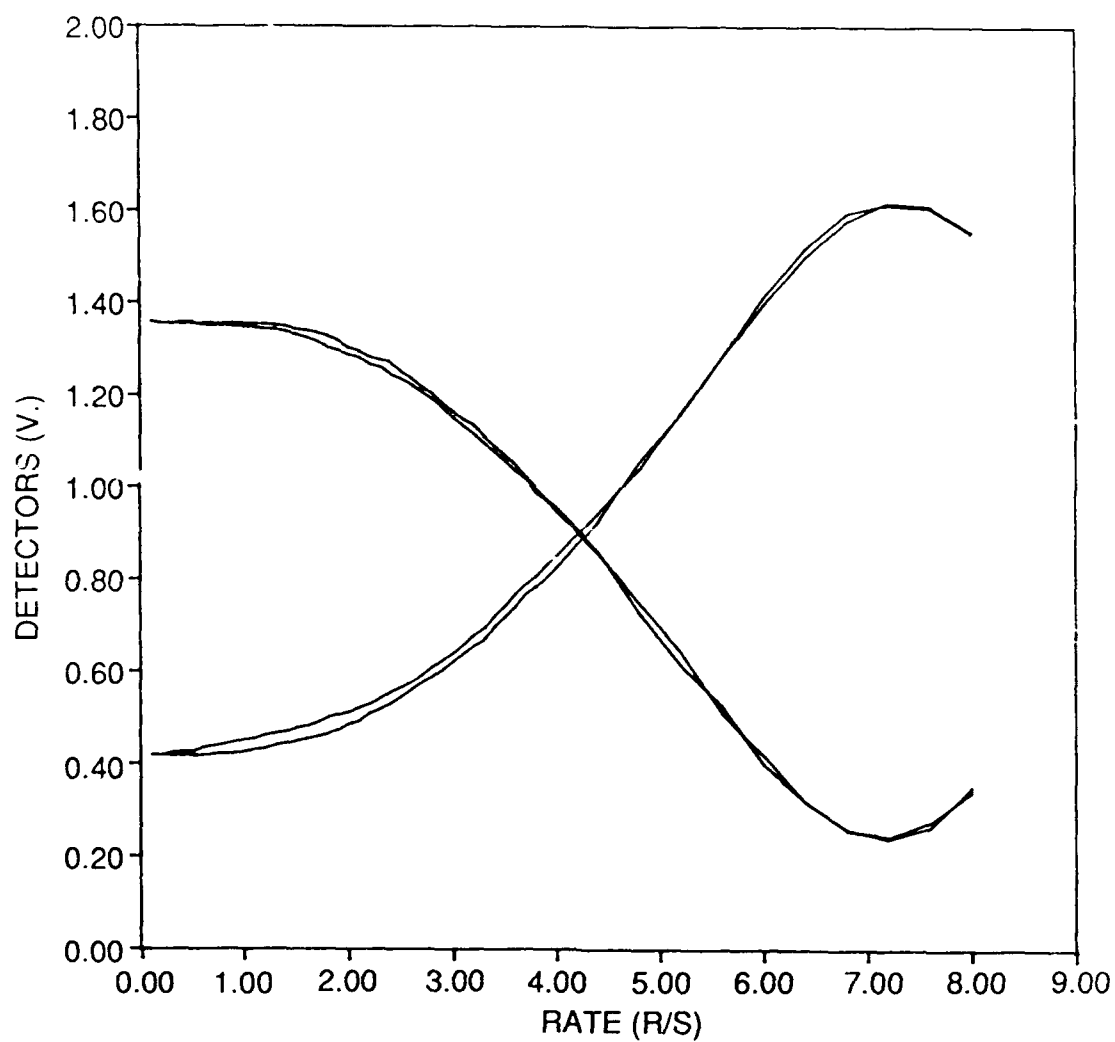
Figure 10. Individual detector outputs from the sensor test
bed show optical transmission increasing for one
polarization and decreasing for the orthogonal
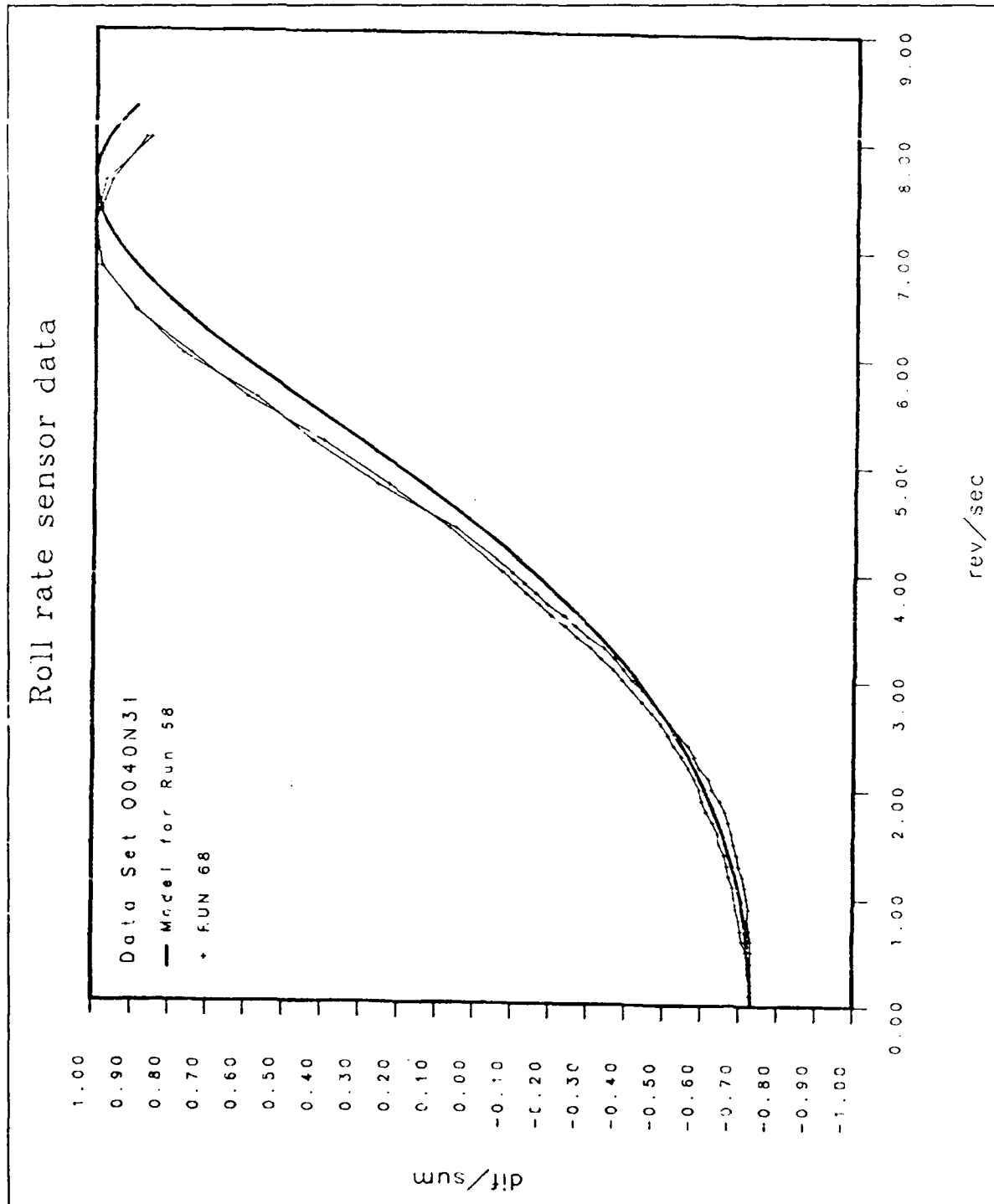polarization while sensor loading increases as a
function of rate.

Figure 11. Data from Run 68 along with the response predicted by the model.
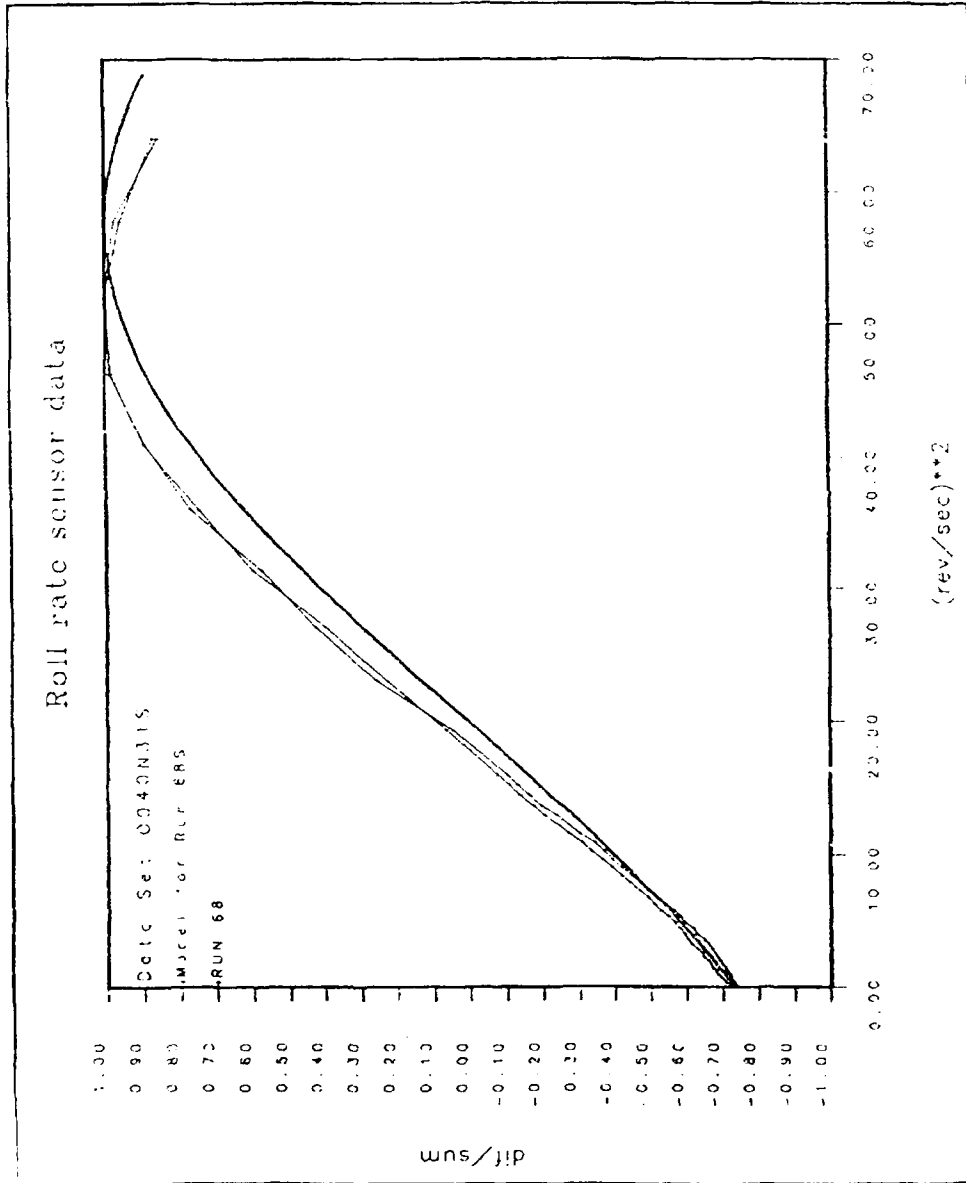
Figure 12. The data from Run 68 shows a linear response between ±0.6 when plotted against rate squared.
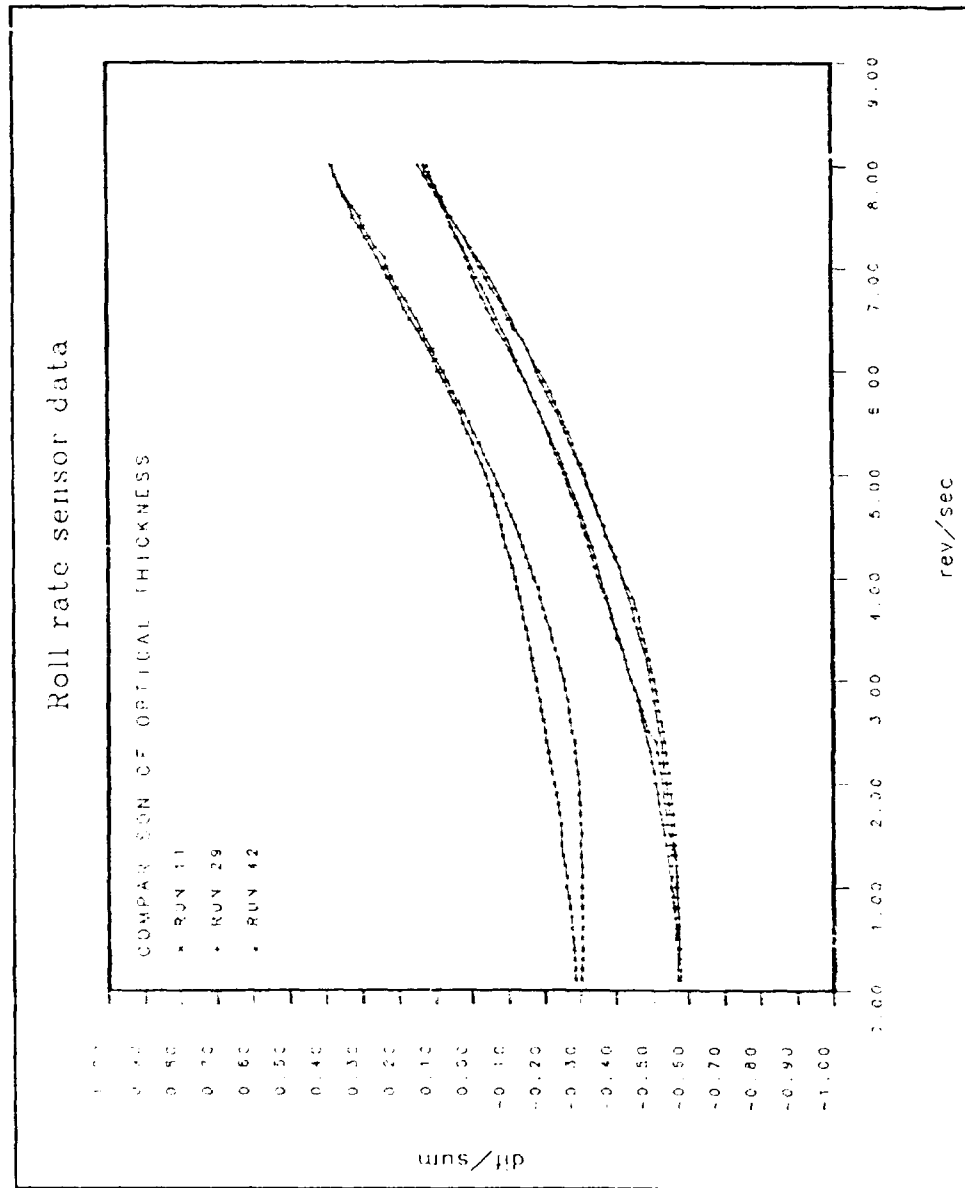
45

Figure 13. Three data sets using similar width sensing elements but having varying optical thickness show sensor response is independent of optical thickness.
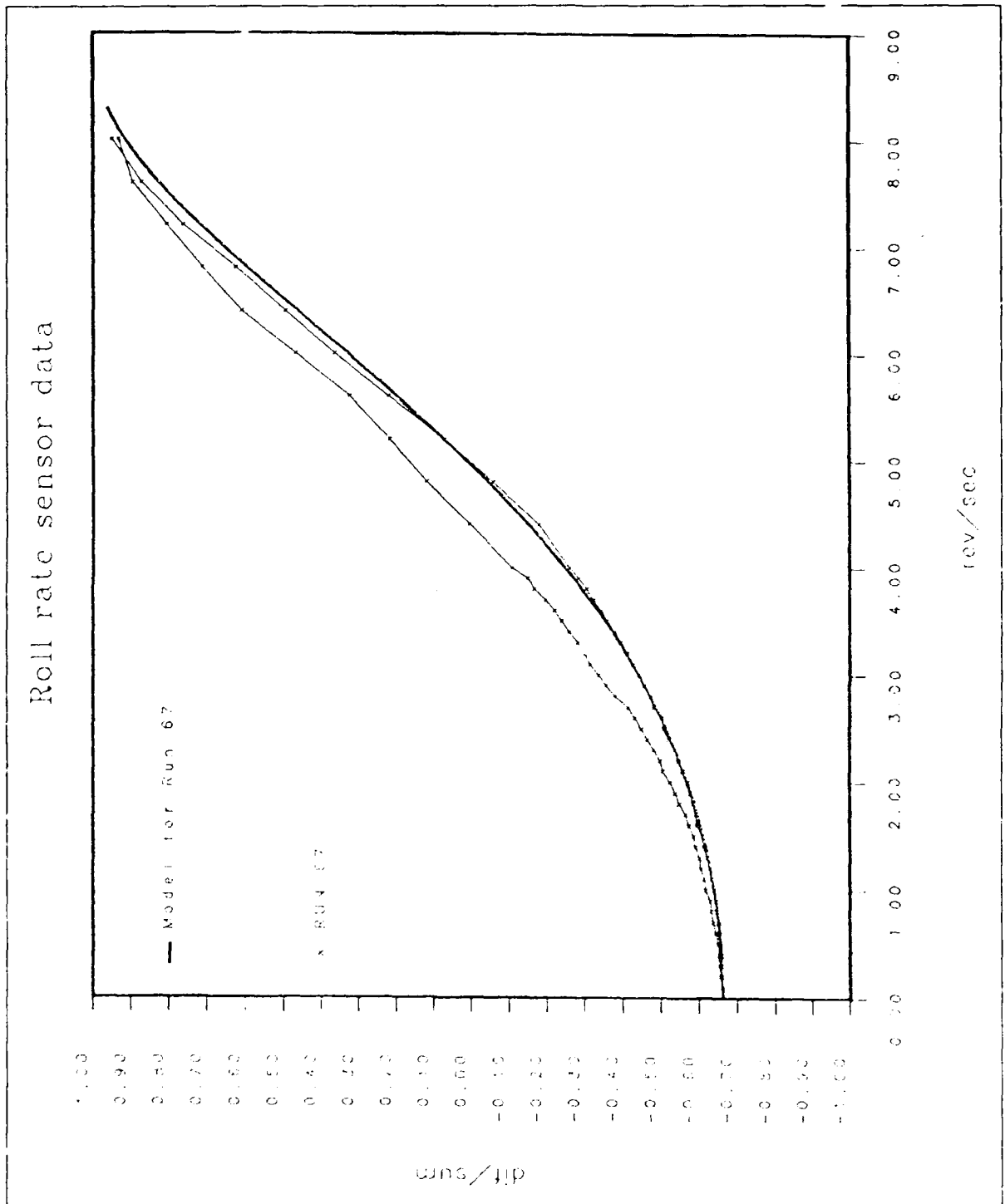
45

Roll rate sensor data

Model for Run 67

Run 67

rev/sec

dif/sum

Fig. 1. The difference/sum output for an alternate photodiode material potential...
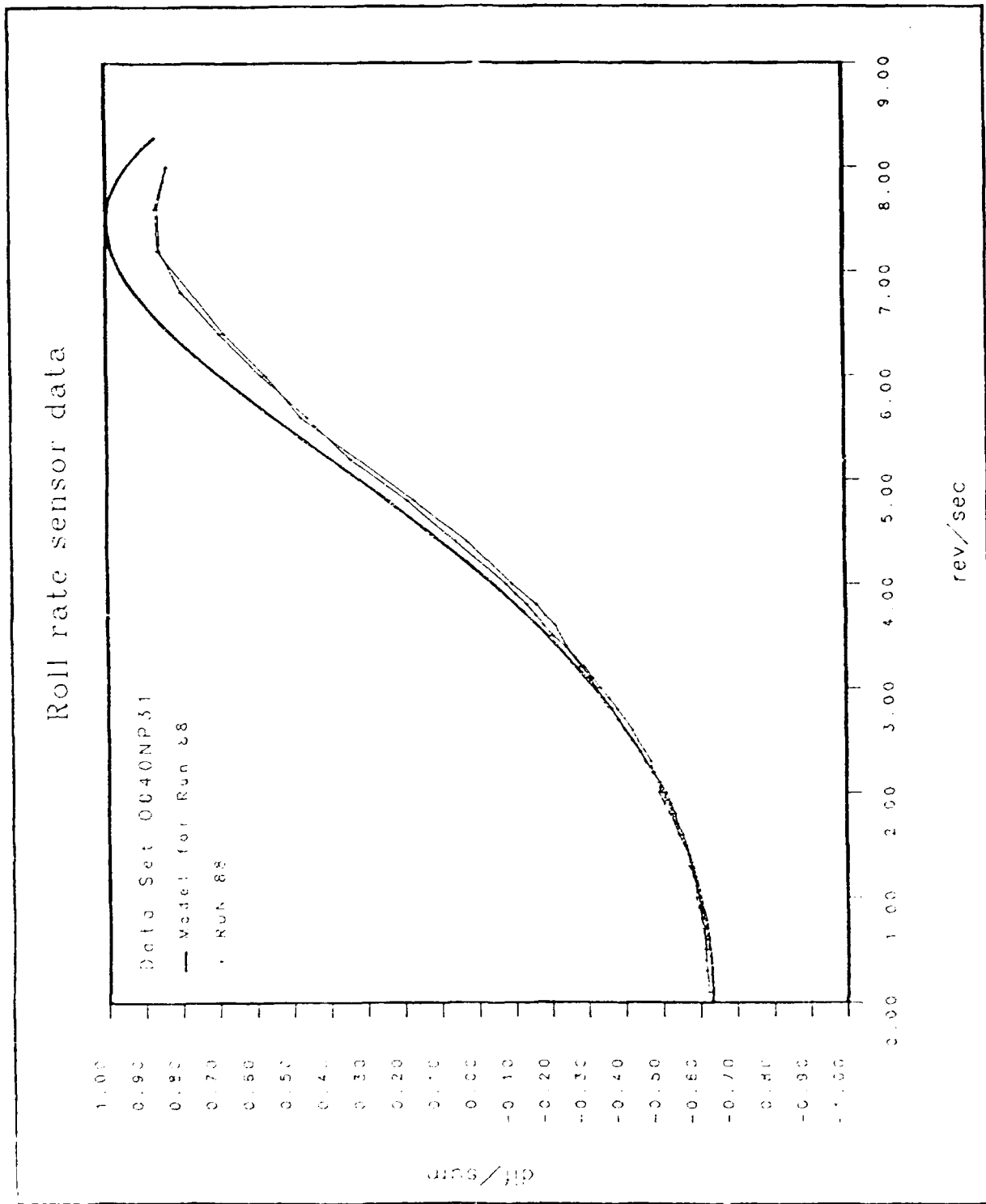
Figure 15. Sensor response for the post type sensing element shows less hysteresis.
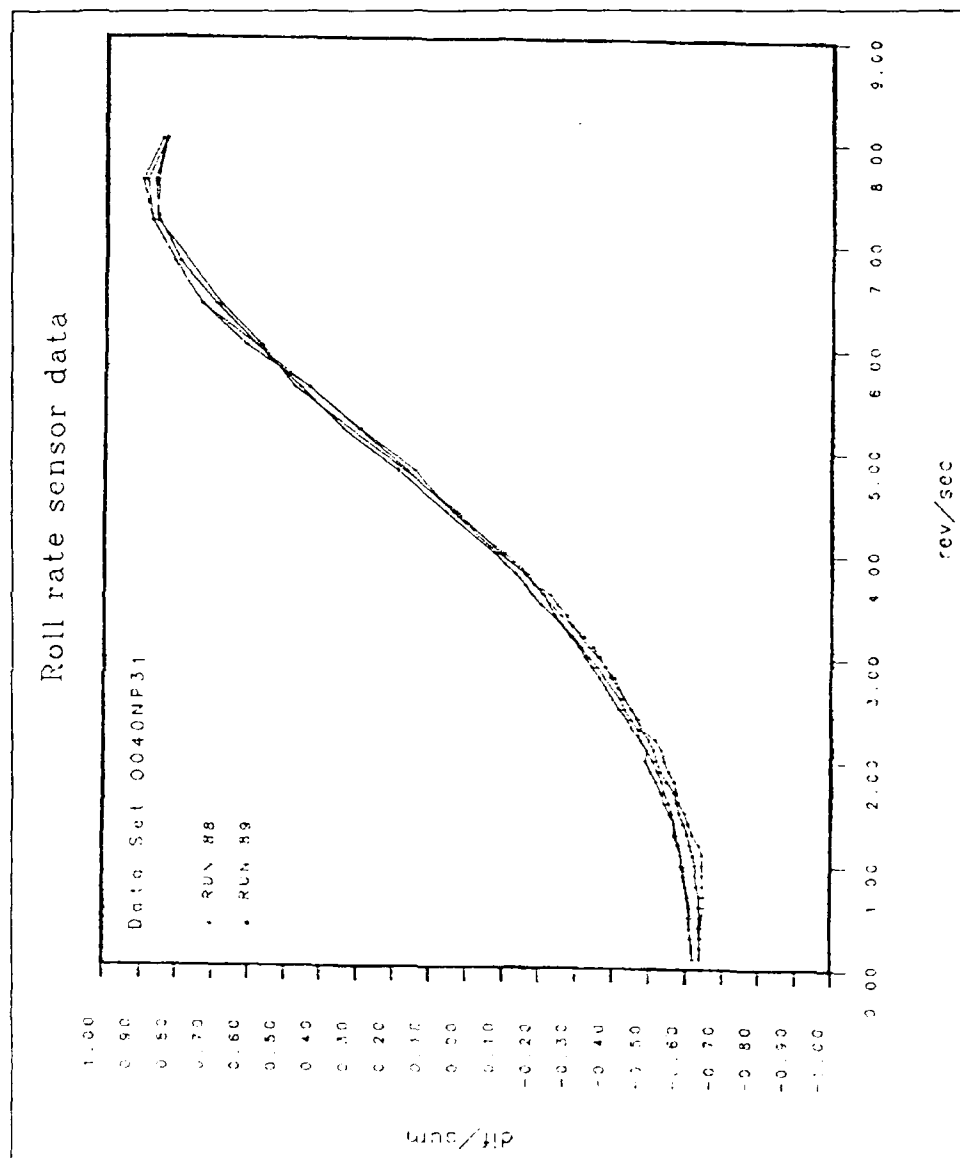
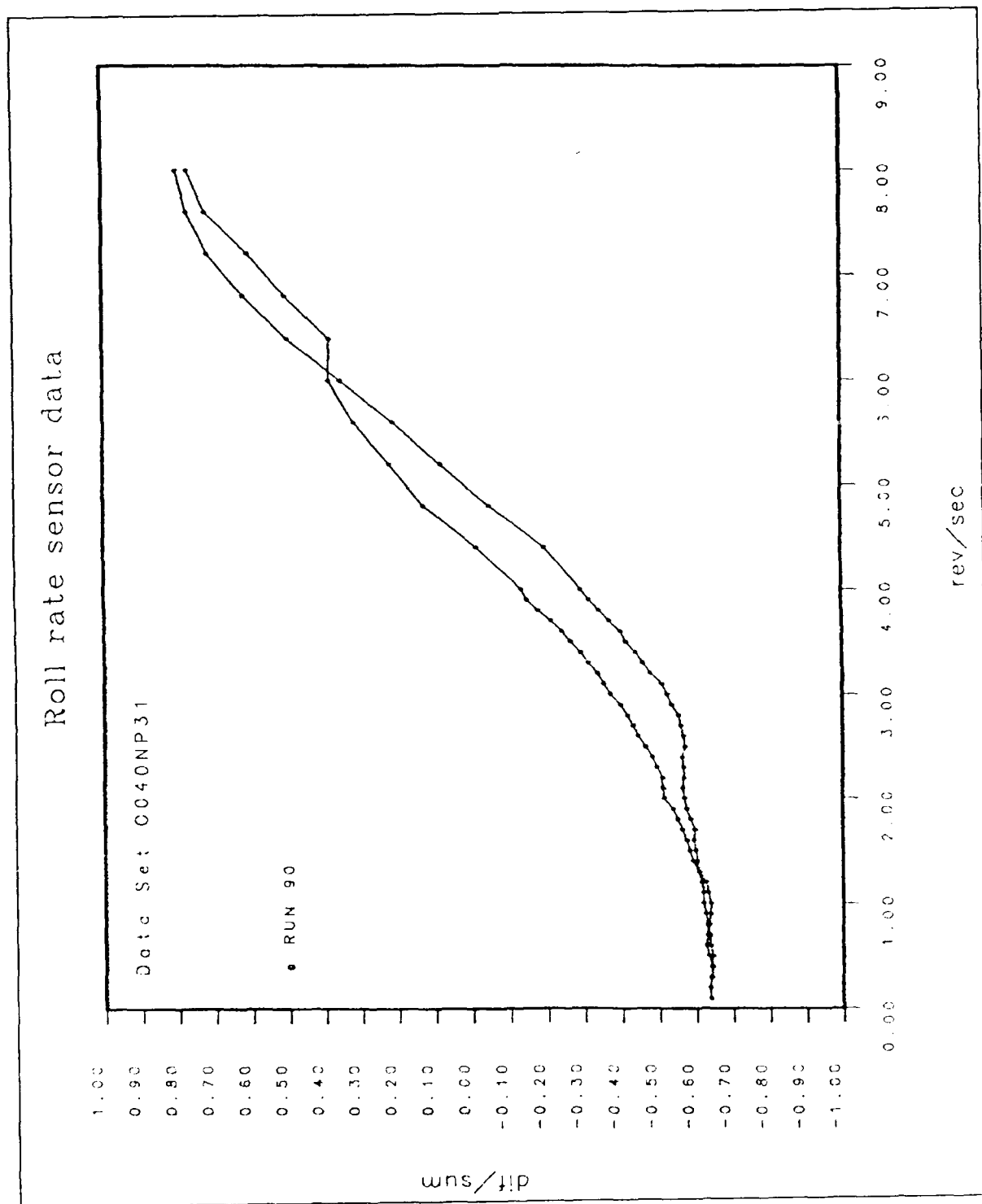Figure 16. Comparison of two consecutive experiments shows repeatability of sensor response.

Figure 17. The same sensor configuration used in Figure 16 shows effects of proof mass settling from sitting over a weekend.

50

RUN 172 S

DIFF/SUM

RATE^2 (REV/SEC)^2
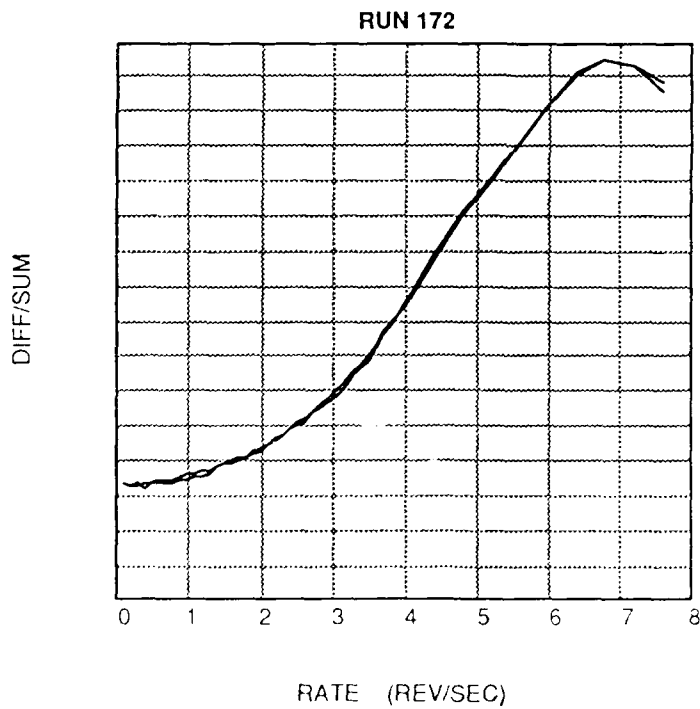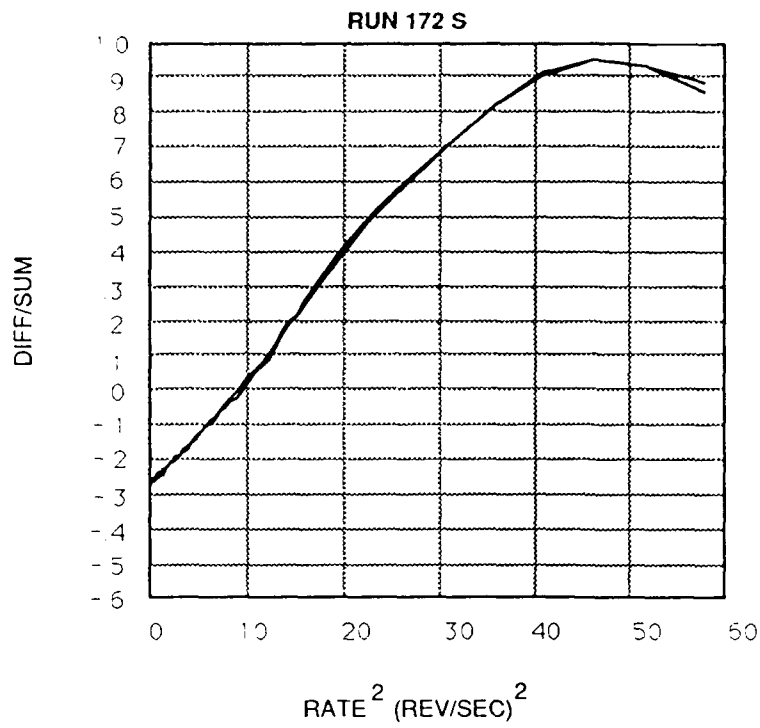
RUN 172

DIFF/SUM

RATE (REV/SEC)

Figure 18.   Run 172 is typical of sensor response for a
zero-clearance sensing element in the sensor test bed
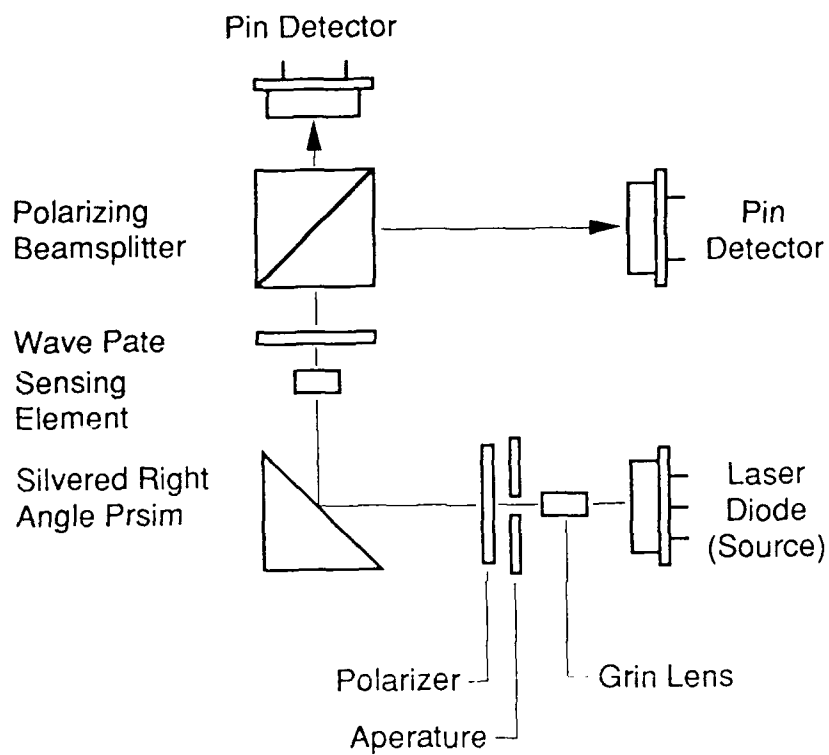utilizing a 31 gram proof mass.

Figure 19. The folded optical path in the prototype
Micro Miniature Roll Rate Sensor reduces
the size required for physical layout and
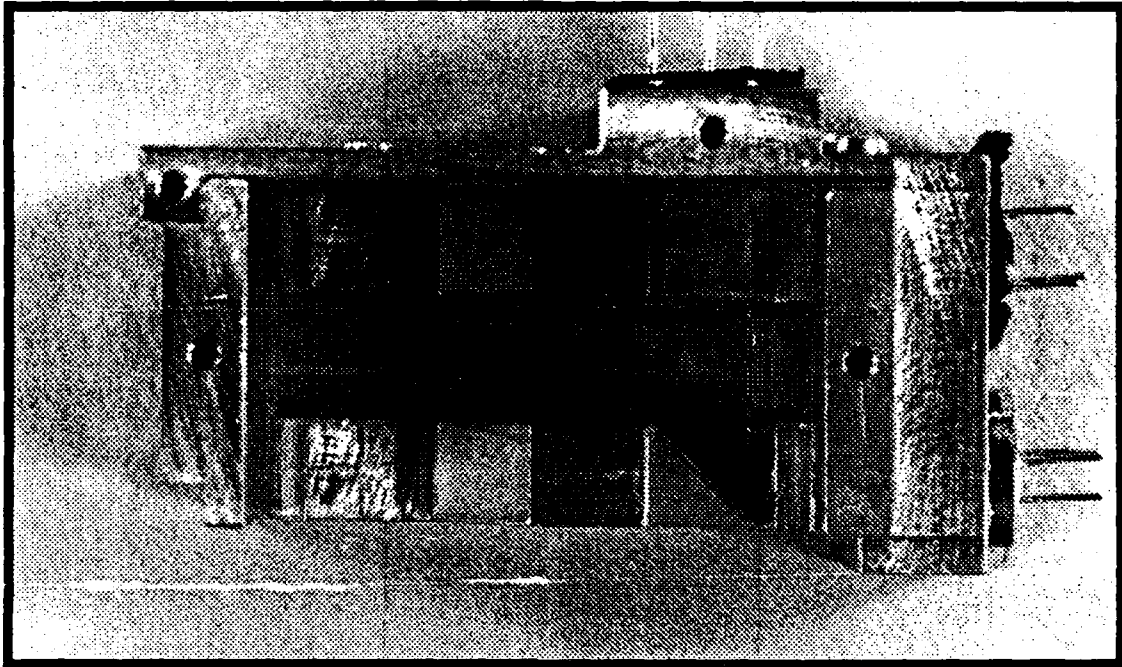localizes electrical connections.

52

Figure 20. Top view of partially assembled Micro Miniature
Roll Rate Sensor with all bulk optic and electro-
optic components installed.
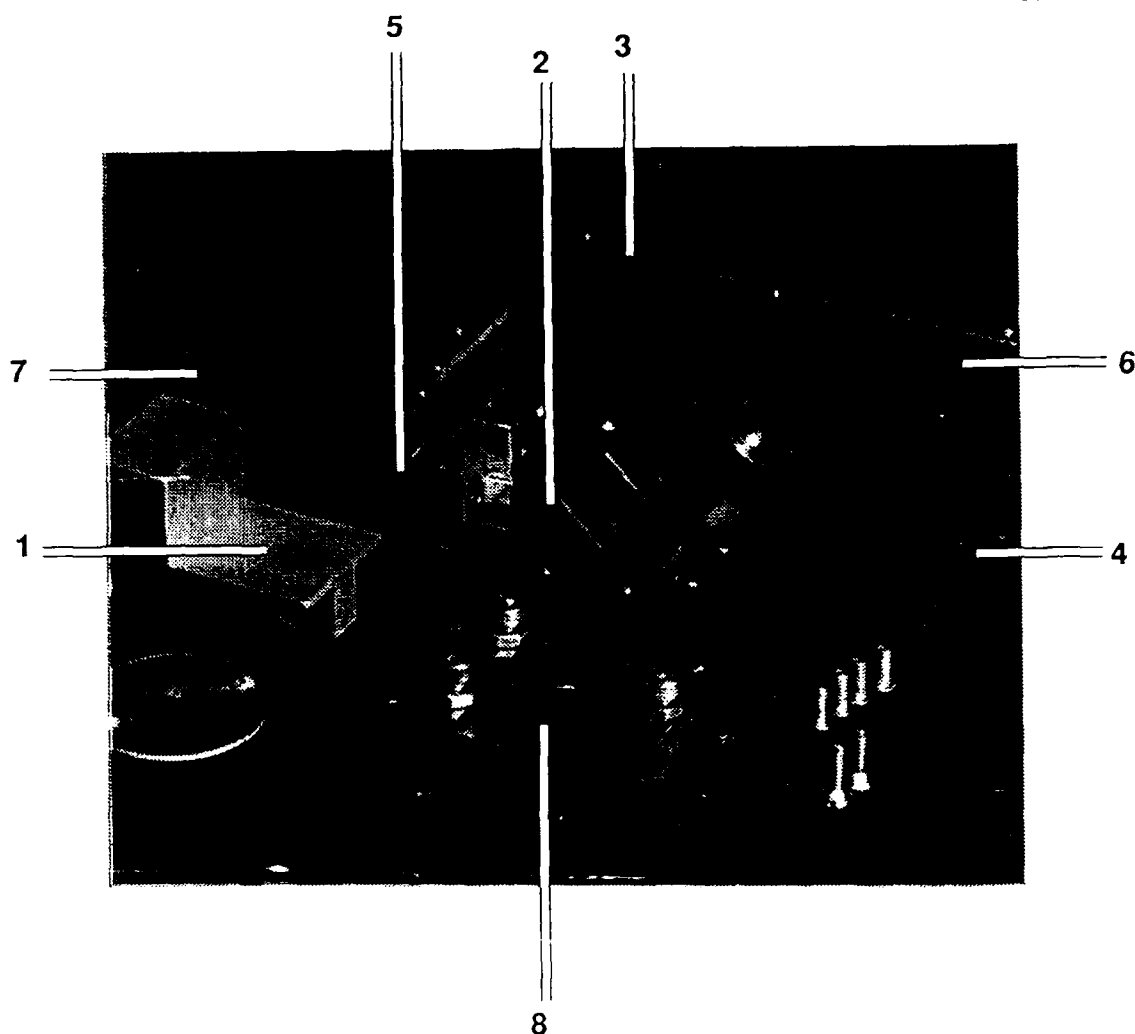
Drawing Set 14213

	Drawing #	Title
1	D-300187	Fixture, Roll Rate Sensor
2	D-300188	Base Plate, Roll Rate Sensor
3	D-300189	Back Plate, Roll Rate Sensor
4	D-300190	Components, Roll Rate Sensor
5	D-300191	Optics Fixture, Roll Rate Sensor
6	D-300192	Left Side Panel, Roll Rate Sensor
7	D-300193	Right Side Panel, Roll Rate Sensor
8	D-300194	Top Panel, Roll Rate Sensor
	D-300196	Assembly, Roll Rate Sensor

Figure 21. Components of the prototype Micro Miniature Roll
Rate Sensor and the associated mechanical drawing
set.
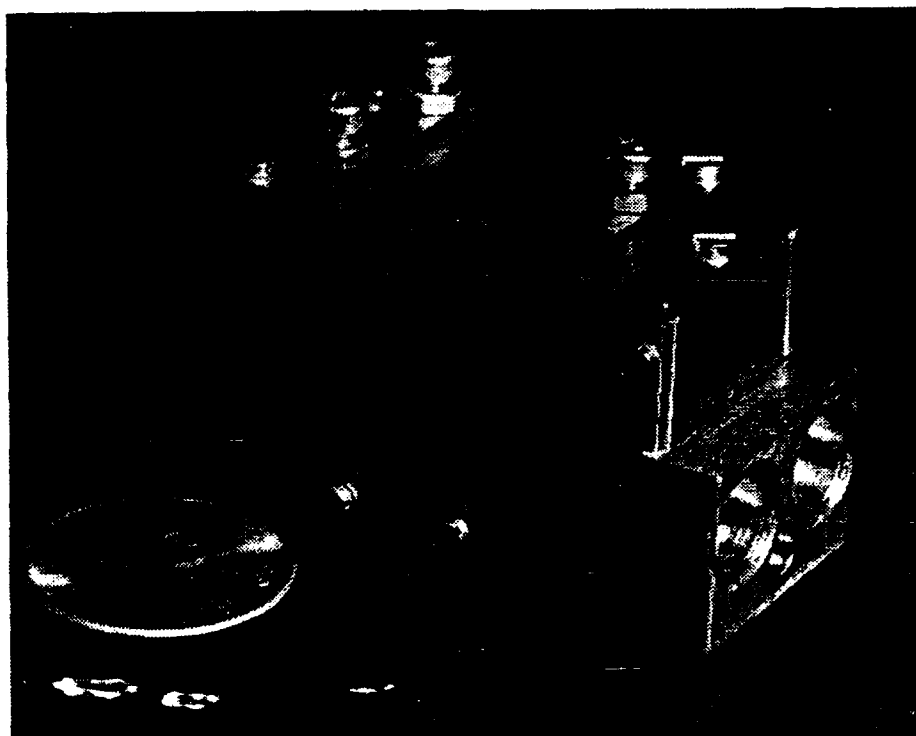
Figure 22. View of the Assembled Micro Miniature Roll Rate
Sensor with No Electro-Optic Components Installed.

Housing Containing MRRS

Sensor Electronics

Rate Table Plate
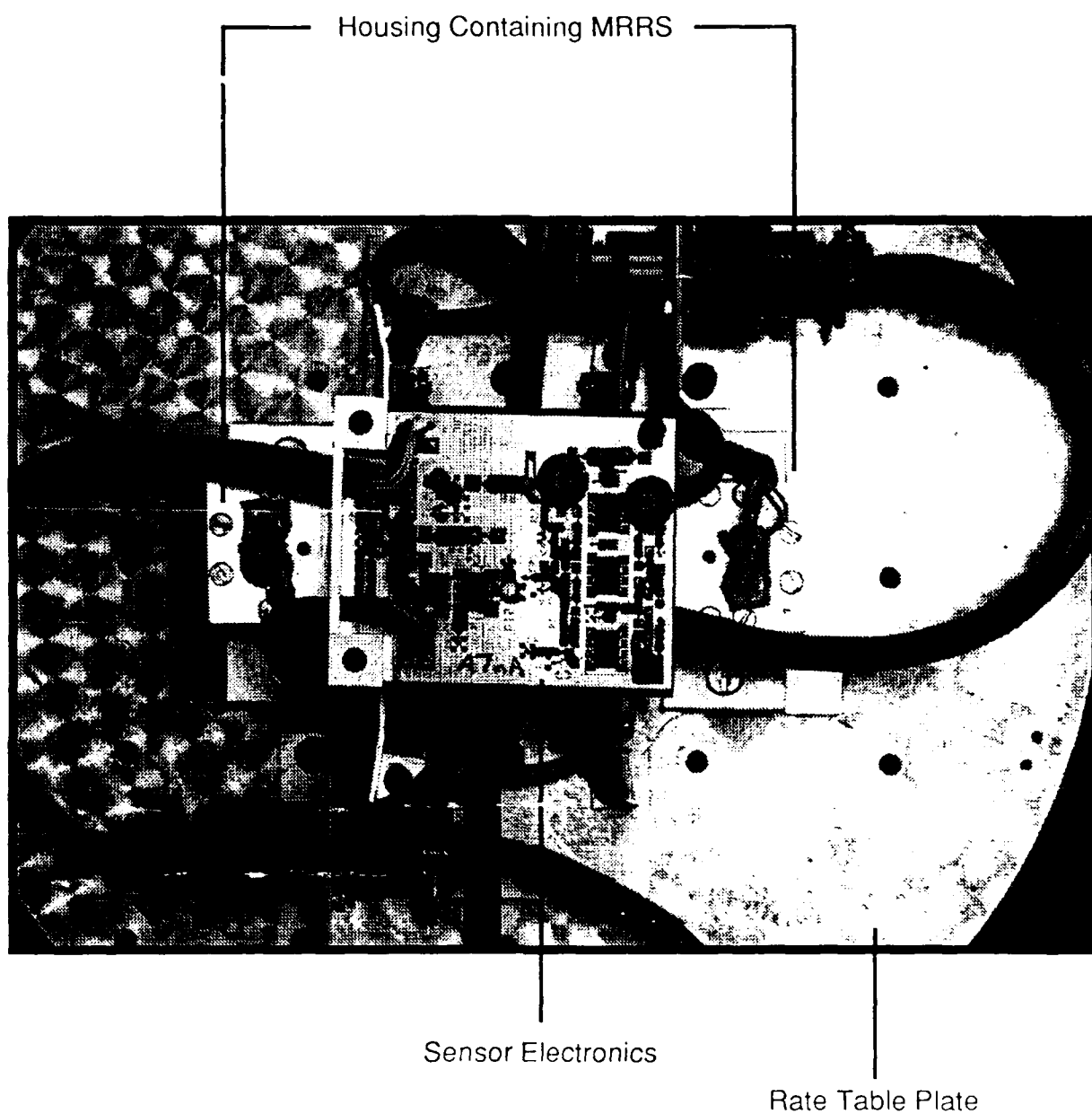
Figure 23. Top view of a pair of Micro Miniature Roll Rate Sensors
and the associated electronics mounted on rate table.
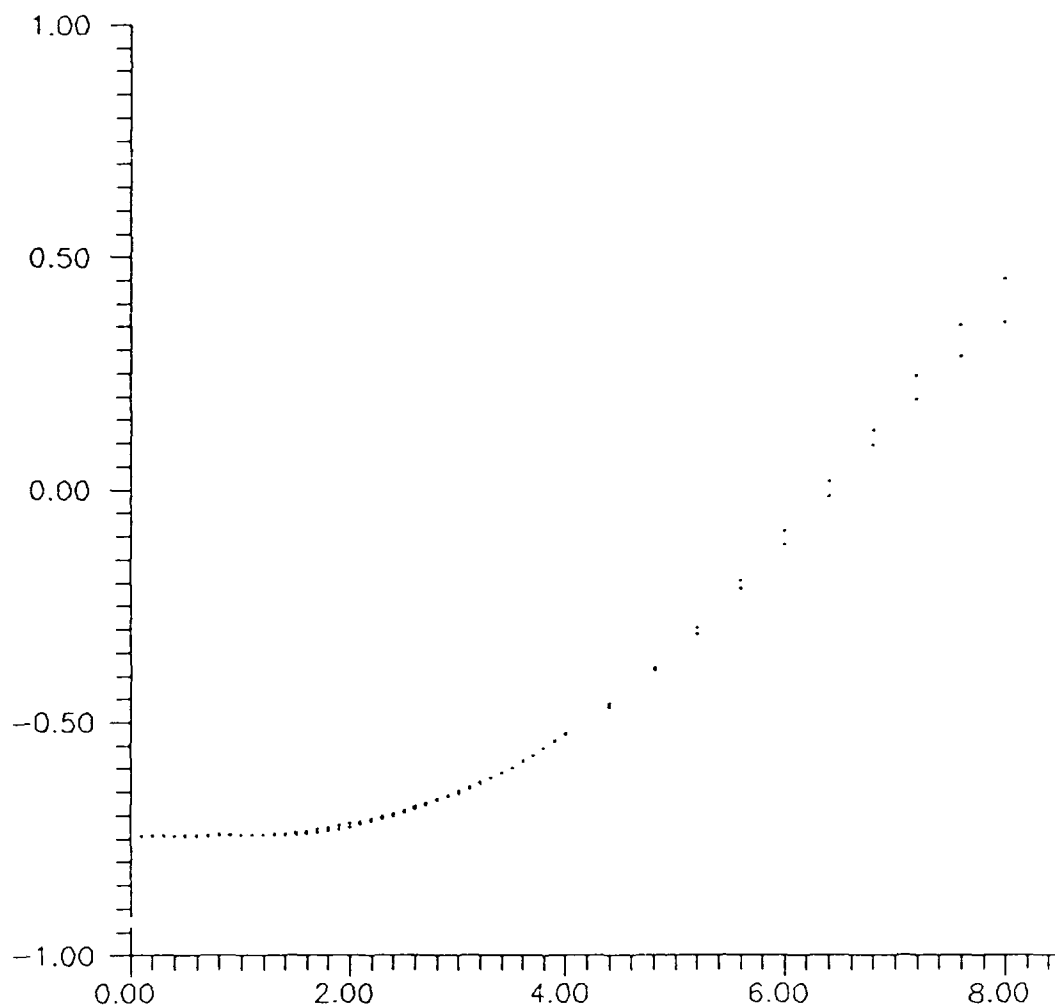
Figure 24. Data from Run 177 showing difference/sum output
of prototype MRRS #1.

$w \equiv 2.04 \cdot mm$

$wp \equiv 140 \cdot nm$

$pm \equiv 51.2 \cdot g$

$\Gamma wp = 1.128 \cdot rad$

$f = 1.069 \cdot 10^{4} \cdot fc$
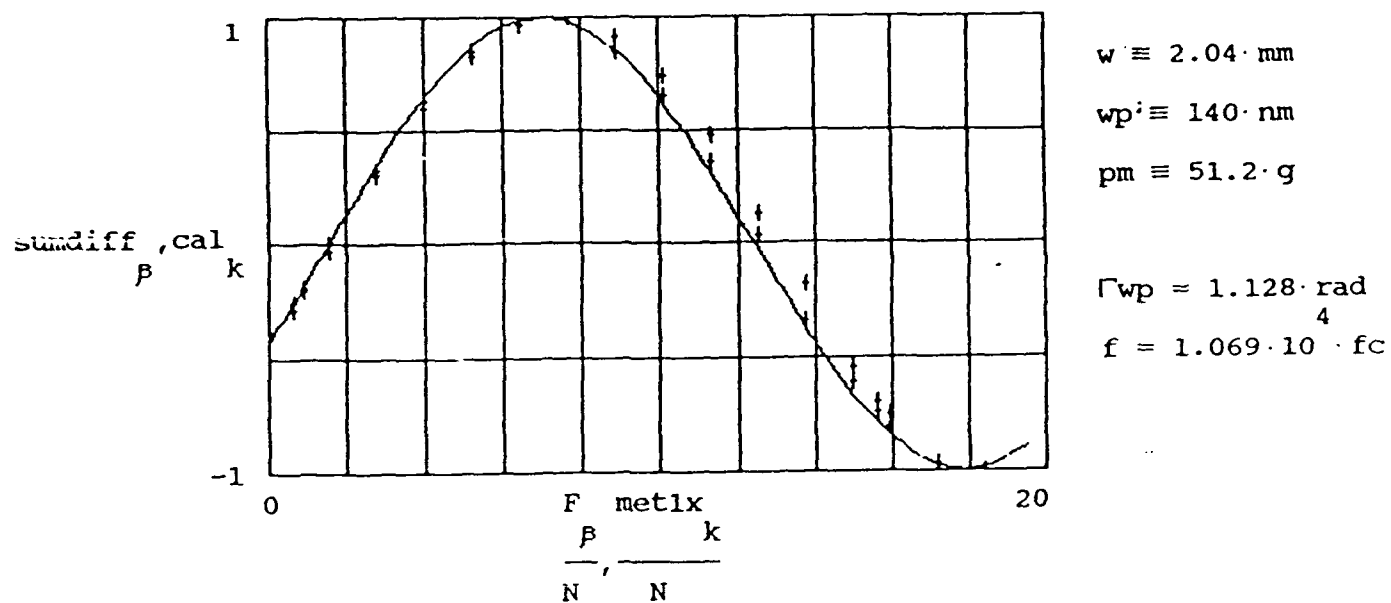
Figure 25. Comparison of MATHCAD model predictions
            (line) to pretest calibration data points
            (pluses) for Sensor 2.

STA5QB — Sensor 1   1000 deg/sec.
7/28/89
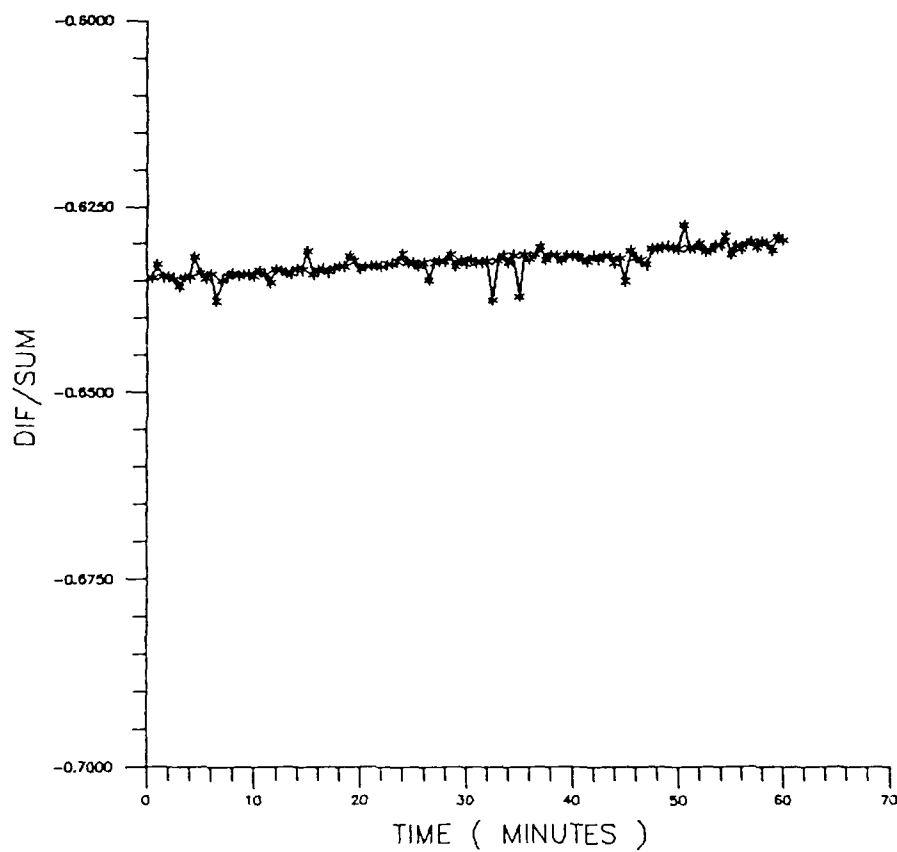
Figure 26.   Stability test of Sensor 1 at a rate of
1000 deg/sec.

59
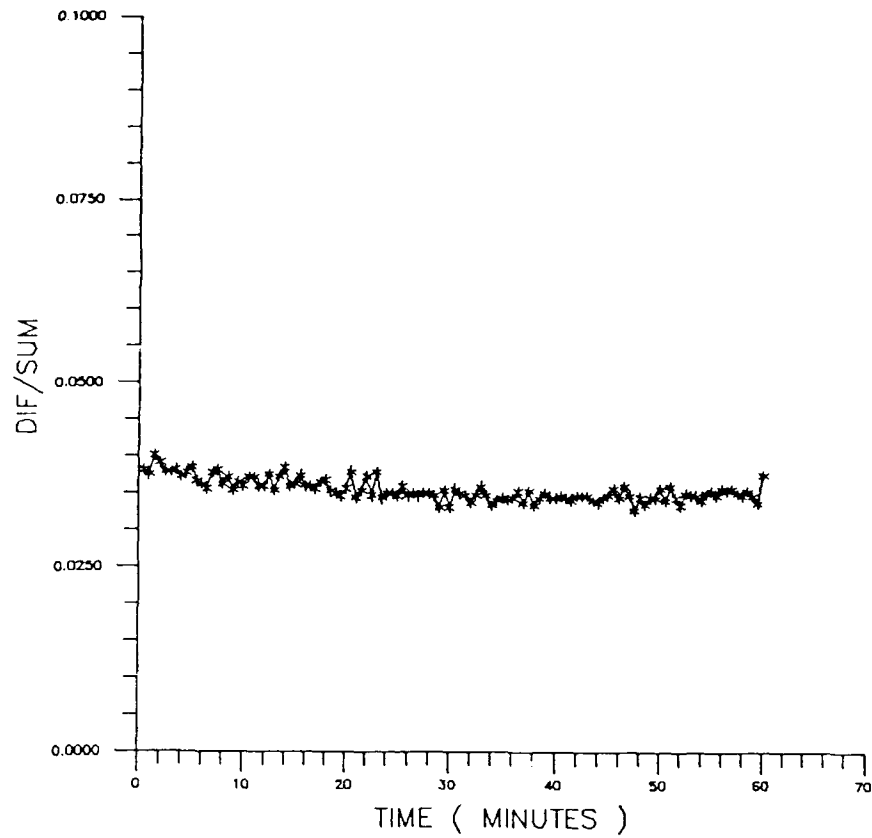
Figure 27.   Stability test of Sensor 2 at a rate of
1500 deg/sec.

RUN202AB — Quick DIF/SUM Outputs for
Sensors 1 and 3.   Spin CW.   7/28/89
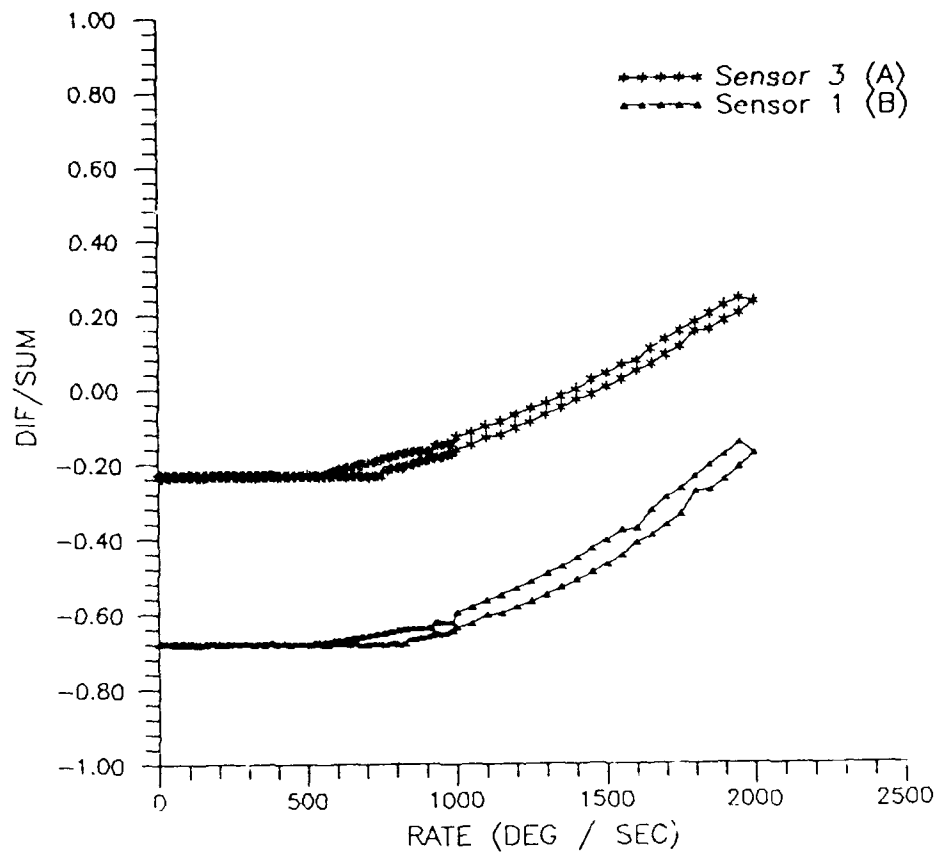
Figure 28.   Experimental data showing outputs for Sensors
1 and 3.

Summary of Quick DIF/SUM Outputs for
Sensors 2 and 4 showing aata acquired
at ARDEC 7/27-28/89.
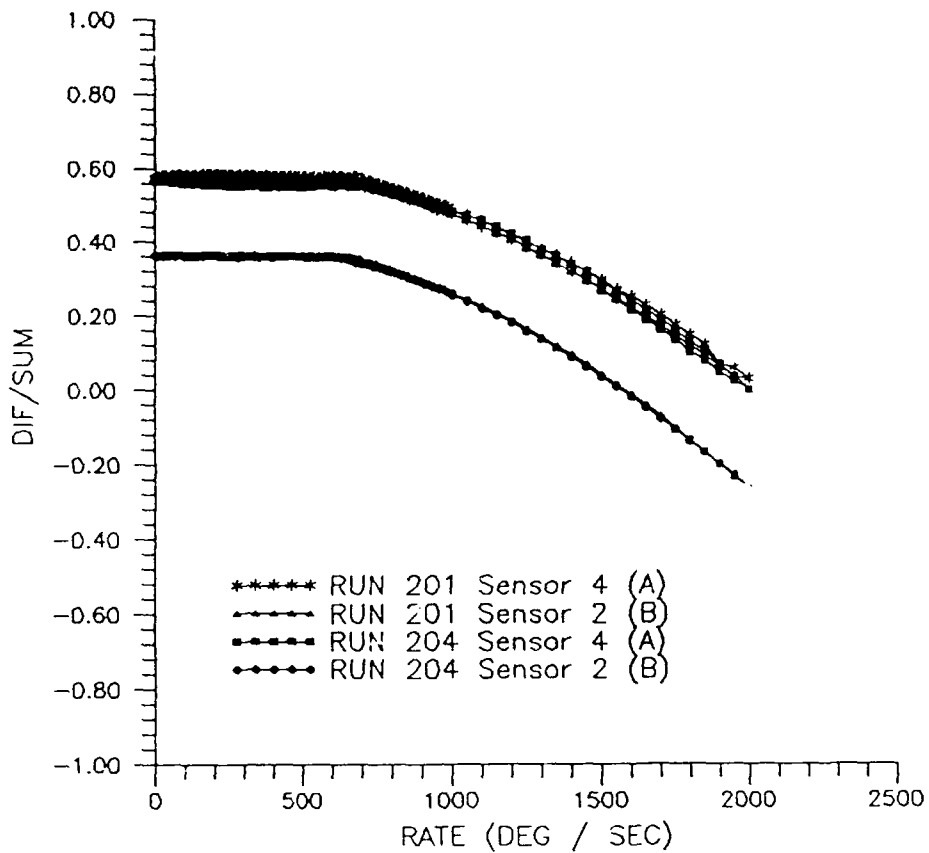
Figure 29.   Two pairs of experimental daca showing outputs for
Sensors 2 and 4.

APPENDIX A

CONFIGURATION ITEM DEVELOPMENT
SPECIFICATION FOR THE MICRO-MINIATURE
ROLL RATE SENSOR

1.   SCOPE

1.1 This specification establishes the development goals for a Micro-Miniature Roll Rate Sensor for use in guided munitions such as the XM712 guided 155mm projectile (Copperhead), under the Phase II SBIR Contract Number DAAA21-87-C-0066.

2.   APPLICABLE DOCUMENTS

2.1 Performance specifications have been established from Military Specification MIL-P-63234(AR) - Projectile, Guided, 155mm, XM712, Roll Rate Sensor for.

2.2 Drawings developed under Contract Number DAAA21-87-C-0066 and submitted to the Contracting Officer's Technical Representative (COTR) at the completion of all work, detail the development design.

2.3 Theoretical background and experimental development are described in the Scientific and Technical Report Summary, GC-TR-88-1702, Micro-Miniature Roll Rate Sensor, submitted under Contract Number DAAA21-87-C-0066.

3.   REQUIREMENTS

3.1 Item definition. The Micro-Miniature Roll Rate Sensor (MRRS) is an angular rate sensor used to sense projectile roll rate. Contained in the MRRS is a polarized optical beam passing through a photoelastic (birefringent) sensing element, which is subsequently split into orthogonal polarizations and detected by PIN diodes. The photoelastic sensing element is loaded with a proof mass.

64

Angular rate inputs to the MRRS result in loading of the sensing element determined by the proof mass under the force of centripetal acceleration. The difference signal of the PIN diodes is divided by the sum of the two diodes to provide an intensity invariant signal proportional to angular rate squared. Use of two sensors with different proof mass and/or photoelastic sensing elements may be utilized to provide extended resolution over large rate changes.

3.2   CHARACTERISTICS

3.2.1 Performance. The development goals for the MRRS are to meet the operational requirements of MIL-P-63234(AR) with respect to rate measurement after launch shock, and to demonstrate the feasibility of meeting the physical dimensional specifications with the operational prototype sensor.

3.2.1.1 Rate measurement specification. The MRRS shall perform rate measurement over the range of 0-2000 deg/sec with an accuracy of 1 deg/sec. Testing will be performed at an Army approved rate testing facility.

3.2.1.2 Launch shock requirements. The MRRS shall withstand, and meet the measurement specification of 3.2.1.1, following exposure launch acceleration of 9000 ± 300 g forward along the input axis of the MRRS.

3.2.1.3 Dimensional specification. The MRRS must fit inside a cylindrical package with a maximum radius of 2.575" and a maximum height (in the direction of flight) of 1.205". The prototype MRRS may exceed the height dimension for the purposes of using standard off-the-shelf components in the prototype design, but must demonstrate the feasibility that sufficiently compact final design are achievable.

3.2.2   Electrical requirements.   The electronic circuitry as-
sociated with the prototype MRRS must provide buffer signal outputs
from the PIN detectors and provide reasonable signal levels for
data acquisition equipment, as defined in section 3.2.2.1.
Circuitry must also be provided for control of an optical source
as defined in section 3.2.2.2.

3.2.2.1 Signal output specifications.   The signals from the MRRS
electronics must have an output impedance of 50 ohms, and have
sufficient gain to source output signals in excess of 1 volt.
These signals shall track the intensities of the PIN detectors with
a bandwidth of at least 100 KHz.

3.2.2.2   Current source specifications.   The current source
circuitry for the optical source must be capable of supplying up
to 100 mA at 2 V, and must incorporate slow start circuitry. The
circuit will be closed loop type where the output current is
controlled by a monitor current of .3 to 3.7 mA.

3.2.2.3   Power requirements.   The MRRS electronics must operate
from ± 12V and + 5 V.

APPENDIX B

MATHCAD COMPUTER MODEL

This file allows manipulation of the roll rate sensor parameters while observing changes in output. The proof mass is set up as an array of masses m(i). Variations of the sensor output can be observed by adjusting any parameters such as w for width of photoelastic material, or wavelength λ foreffects on the optical bias of the system. Note that wavelength effects are not accounted for in the fringe constant of the sensing element; the value used was experimentally determined at 780 nm, and the sensing element will actually become more sensitive at shorter wavelengths and less so at longer ones.

   Units used are those typical for the actual physical components; conversions are performed thru the use of the defined units.

Base Units: $\quad$ cm $\equiv$ 1L $\quad$ g $\equiv$ 1M $\quad$ sec $\equiv$ 1T $\quad$ rad $\equiv$ 1

Derived Units: $\quad$ m $\equiv$ 100·cm $\qquad$ mm $\equiv$ 0.1·cm $\qquad$ nm $\equiv$ 0.001·mm

$$kg \equiv 1000 \cdot g$$

$$deg \equiv \frac{\pi}{180} \cdot rad$$

$$N \equiv \left[\frac{kg \cdot m}{sec^2}\right]$$

$$ms \equiv .001 \cdot sec$$

$$Pa \equiv \left[\frac{N}{m^2}\right]$$

$$fc \equiv Pa \cdot m$$

Parameter definitions:

Rate: $\qquad\qquad \beta := 1 \,..288$ $\qquad\qquad\qquad$ Rate range increment.

$$\omega_\beta := 10 \cdot \beta \cdot \frac{deg}{sec}$$ $\qquad$ Rate range

Proof mass: $\qquad$ i := 0 ..5 $\qquad\qquad\qquad\quad$ Dimension of proof mass array

$$m_i := 25 \cdot g + i \cdot 5 \cdot g$$ $\qquad$ Proof mass range.

r := 5·cm $\qquad\qquad\qquad\qquad$ Radial distance to center of gravity of proof mass.

Sensing element: $\quad$ w := 1·mm $\qquad\qquad\qquad$ Width range of sensing element.

f := 10693·fc $\qquad\qquad\qquad$ Fringe constant.

Waveplate: $\qquad$ wp := 140·nm $\qquad\qquad\qquad$ Retardance of the waveplate.

λ := 780·nm $\qquad\qquad\qquad\quad$ Operating wavelength.

$$\Gamma wp := 2 \cdot \pi \cdot rad \cdot \frac{wp}{\lambda}$$ $\qquad$ Birefringence of the waveplate.

$$\Gamma_{i,\beta} := \frac{2 \cdot \pi \cdot rad \cdot r \cdot m_i \cdot \left[\omega_\beta\right]^2}{f \cdot w}$$

Birefringence due to radial acceleration.

$$sumdiff_{i,\beta} := -cos\left[\Gamma_{i,\beta} + \Gamma wp\right]$$
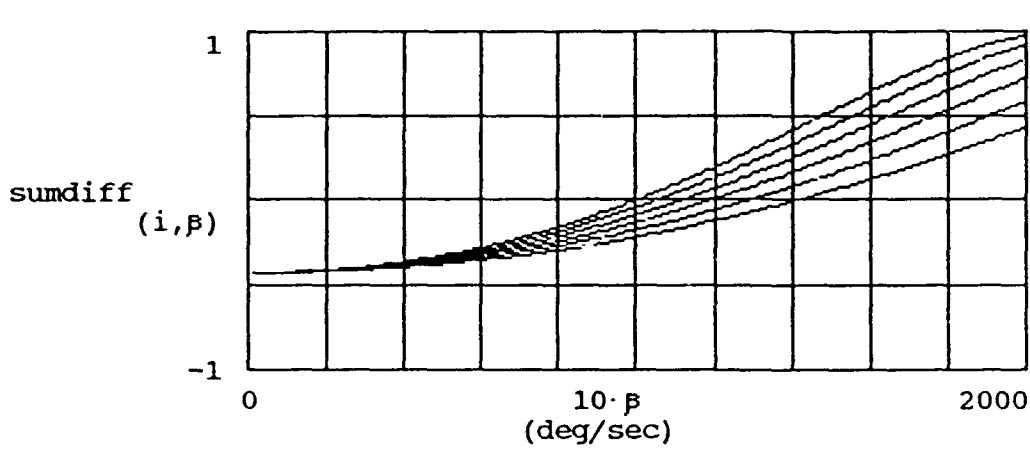
m_i
$\frac{1}{25 \cdot mass}$
$\frac{1}{30 \cdot mass}$
$\frac{1}{35 \cdot mass}$
$\frac{1}{40 \cdot mass}$
$\frac{1}{45 \cdot mass}$
$\frac{1}{50 \cdot mass}$

69

APPENDIX C

SUPPORT ELECTRONICS

Chan 1 in

C1 100 pf
R2 4.12K
2
3
1/2 AD648
U1
1
R1 4.12K

R3 1.00K
TP1

C2 120 pf
R4 2.00K
2
3
1/2 AD648
U2
1
R5 2.00K

R6 10.0K
TP2

3
2
1/2 AD648
U3
1

V_D
R5 47 Ω 1W
Q1 2N2222
Chan 1 Out

R7 1M

Chan 2 in

C3 100 pf
R10 4.12K
6
5
1/2 AD648
U1
7
R11 4.12K

R12 1.00K
TP3

C4 120 pf
R13 2.00K
6
5
1/2 AD648
U2
7
R14 2.00K

R15 10.0K
TP4

5
6
1/2 AD648
U3
7

V_D
R17 47 Ω 1W
Q2 2N2222
Chan 2 Out

R16 1M

V_D
8
U1
4
V_S
C8 .1 µf 25V
C9 .1 µf 25V

V_D
8
U2
4
V_S
C13 .1 µf 25V
C14 .1 µf 25V

V_D
8
U3
4
V_S
C15 .1 µf 25V
C16 .1 µf 25V

V_cc
R21 4.12K

To Laser Diode (LT022)
R20 20Ω 1W

C11 .1µf 10V
V_cc
C12 22µf 25V

8 V_cc   7 CAP   6 GND   5 CTRL
U4 Sharp IR3C01
1 DRIVE   2 PIN IN   3 ADJ   4 V_DD

R19 15K
V_S
C10 .1µf 25V

+12V → V_D
+5V → V_cc
-12V → V_S

C5 10 µf 25V
C6 10 µf 25V
C7 10 µf 10V

GND

Note:
R9 & R18 not used

ROLL RATE SENSOR ELECTRONICS
LASER DIODE CIRCUIT

71

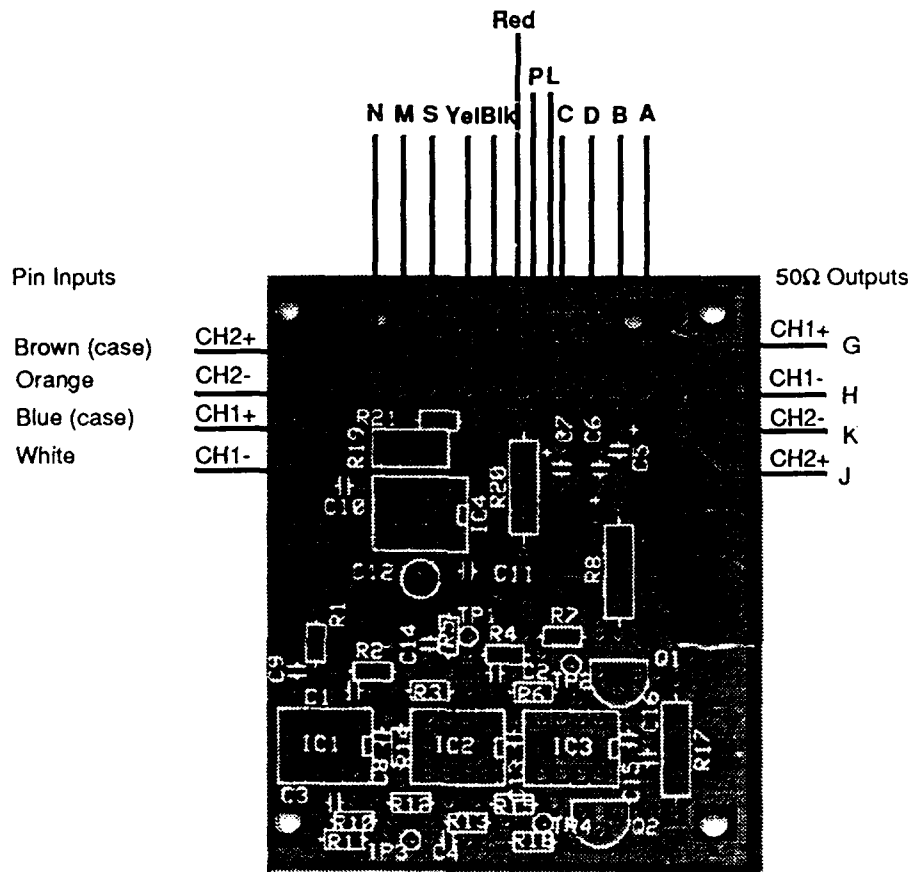# Roll Rate Electronics Connections PC Board to Rate Table Connector
Wiring 12" of 12 Conductor to PW06B14-18P Connector

Red

PL

N M S YelBlk C D B A

Pin Inputs   50Ω Outputs

Brown (case)	CH2+		CH1+	G
Orange	CH2-		CH1-	H
Blue (case)	CH1+		CH2-	K
White	CH1-		CH2+	J

PW06B14-18P

A	Gnd
B	+12V
C	+5V
D	-12V
G	CH1+
H	CH1-
J	CH2+
K	CH2-
S	Gnd
M	LDON
N	PULLUP
P	Gnd
L	Gnd

Commander
Armament Research, Development and Engineering
U.S. Army Armament, Munitions and Chemical Command
ATTN: SMCAR-IMI-I (5) (bldg 59)
            SMCAR-   Insert other ARDEC
            SMCAR-   symbols here
Picatinny Arsenal, NJ   07806-5000

Commander
U.S. Army Armament, Munitions and Chemical Command
ATTN: AMSMC-GCL (D)
Picatinny Arsenal, NJ   07806-5000

Administrator
Defense Technical Information Center
ATTN: Accessions Division (12)
Cameron Station
Alexandria, VA   22304-6145

Director
U.S. Army Materiel Systems Analysis Activity
ATTN: AMSXY-MP
Aberdeen Proving Ground, MD   21005-5066

Commander
Chemical Research, Development and Engineering Center
U.S. Army Armament, Munitions and Chemical Command
ATTN: SMCCR-MSI
Aberdeen Proving Ground, MD   21010-5423

Commander
Chemical Research, Development and Engineering Center
U.S. Army Armament, Munitions and Chemical Command
ATTN: SMCCR-RSP-A
Aberdeen Proving Ground, MD   21010-5423

Director
Ballistic Research Laboratory
ATTN: AMXBR-OD-ST
Aberdeen Proving Ground, MD   21005-5066

Chief
Benet Weapons Laboratory, CCAC
Armament Research, Development and Engineering Center
U.S. Army Armament, Munitions and Chemical Command
ATTN: SMCAR-CCB-TL
Watervliet, NY 12189-5000

Commander
U.S. Army Armament, Munitions and Chemical Command
ATTN: smcar-esp-1
Rock Island, IL 61299-6000

Director
U.S. Army TRADOC Systems Analysis Activity
ATTN: ATAA-SL
White Sands Missile Range, NM 88002